The Astrophysical Journal, 703:1107–1122, 2009 September 20 doi:10.1088/0004-637X/703/1/1107

COSMIC EVOLUTION OF STAR FORMATION IN TYPE-1 QUASAR HOSTS SINCE $z = 1$

Yong Shi[1], George H. Rieke[1], Patrick Ogle[2], Linhua Jiang[1], and Aleksandar M. Diamond-Stanic[1]
[1] Steward Observatory, University of Arizona, 933 N Cherry Ave., Tucson, AZ 85721, USA
[2] Spitzer Science Center, California Institute of Technology, Mail Code 220-6, Pasadena, CA 91125, USA
Received 2009 May 4; accepted 2009 August 6; published 2009 September 4

ABSTRACT

We present *Spitzer* Infrared Spectrograph observations of a complete sample of 57 Sloan Digital Sky Survey type-1 quasars at $z \sim 1$. Aromatic features at 6.2 and/or 7.7 μm are detected in about half of the sample and show profiles similar to those seen in normal galaxies at both low and high redshift, indicating a star formation origin for the features. Based on the ratio of aromatic to star formation infrared (SFIR) luminosities for normal star-forming galaxies at $z \sim 1$, we have constructed the SFIR luminosity function (LF) of $z \sim 1$ quasars. As we found earlier for low-redshift Palomar-Green (PG) quasars, these $z \sim 1$ quasars show a flatter SFIR LF than do $z \sim 1$ field galaxies, implying the quasar host galaxy population has on average a higher star formation rate (SFR) than the field galaxies do. As measured from their SFIR LF, individual quasar hosts have on average LIRG-level SFRs, which mainly arise in the circumnuclear regions. By comparing with similar measurements of low-redshift PG quasars, we find that the comoving SFIR luminosity density in quasar hosts shows a much larger increase with redshift than that in field galaxies. The behavior is consistent with pure density evolution since the average SFR and the average SFR/BH accretion rate in quasar hosts show little evolution with redshift. For individual quasars, we have found a correlation between the aromatic-based SFR and the luminosity of the nuclear radiation, consistent with predictions of some theoretical models. We propose that type-1 quasars reside in a distinct galaxy population that shows elliptical morphology but that harbors a significant fraction of intermediate-age stars and is experiencing intense circumnuclear star formation.

Key words: galaxies: active – galaxies: nuclei – galaxies: starburst

1. INTRODUCTION

Since its discovery, the relationship between the black hole (BH) mass and galaxy bulge properties (Kormendy & Richstone 1995; Magorrian et al. 1998; Gebhardt et al. 2000; Ferrarese & Merritt 2000) has played a critical role in our ideas about galaxy evolution and BH growth. Active galactic nuclei (AGNs), the manifestation of accretion onto BHs, are the main sites of BH growth. The demography of local galaxies suggests that most—perhaps all—massive galaxies host BHs at their centers (e.g., Kormendy & Richstone 1995). The good match between the local BH mass density and the accreted BH mass density in AGNs suggests that the AGN is an indispensable phase of galaxy evolution (e.g., Soltan 1982; Yu & Tremaine 2002; Aller & Richstone 2002; Shankar et al. 2004; Marconi et al. 2004). The interplay between star formation and AGN activity may play a key role in the establishment of the BH–bulge correlation. However, in quasars (luminous AGNs), observational constrains on the BH/star formation relationship are rare due to the difficulty in measuring the star formation rate (SFR) around the bright quasar nuclei.

The host galaxy morphology and colors provide the first insight into the level of star formation. At low redshift ($z < 0.5$), decades of effort have been devoted to imaging the host galaxies of UV/optically selected type-1 quasars (Hutchings et al. 1984; Smith et al. 1986; McLeod & Rieke 1995; Bahcall et al. 1997; Dunlop et al. 2003; Floyd et al. 2004; Guyon et al. 2006). Important technical developments, especially with space-based and adaptive optics (AO) instruments, have provided observations with dramatically improved spatial resolution, stable point-spread functions (PSFs), and large dynamic range, which are keys to extracting quantitative information on host galaxies surrounding the bright AGN. Radio-loud quasars are found to be associated with luminous early-type galaxies with structure parameters indistinguishable from those of quiescent ellipticals (Smith et al. 1986; Dunlop et al. 2003). Radio-quiet quasars reside on average in less luminous galaxies with diverse morphologies that show some dependence on the host and nuclear luminosity, i.e., more frequently of early type for the more luminous nuclei and hosts (McLeod & Rieke 1995; Bahcall et al. 1997; Floyd et al. 2004; Guyon et al. 2006). At $M_B < -23$, roughly 50% of quasar hosts show normal elliptical morphologies (Bahcall et al. 1997; Guyon et al. 2006). The fraction of bright quasar hosts with ongoing merging features is 10%–30% (Bahcall et al. 1997; Guyon et al. 2006). However, this merger fraction may be underestimated especially at the late merging stage where the tidal tails become relatively faint. Such a bias has been demonstrated by the discoveries of merger remnants in quiescent elliptical hosts (Canalizo et al. 2007; Bennert et al. 2008). The merger fraction for near-IR-selected quasars (Cutri et al. 2002) and far-IR excess quasars (Canalizo & Stockton 2001) is much higher (>50%; Canalizo & Stockton 2001; Hutchings et al. 2003; Marble et al. 2003). However, it is unclear if this is because tidal features are relatively easily detected in IR-selected quasars with low nuclear/host-light contrast or if there is an evolutionary difference between quasars selected in the UV/optical and those selected in the IR.

The study of stellar populations in quasar hosts using UV/optical spectra has provided another significant constraint on their star formation properties, mainly through detecting the presence of the young- ($\lesssim$100 Myr), intermediate- (~0.1–1 Gyr) or old- (~10 Gyr) stellar populations. However, in both type-1 and type-2 quasars, the nuclear radiation strongly

dilutes the young stellar features, such as the PCygni UV lines and the 4650 Å WR bump, and dominates the line emission of SFR tracers used for normal galaxies. The mean-age-indicator 4000 Å break and intermediate-age-indicator (∼0.1–1 Gyr) Hδ absorption line also suffer from dilution by nuclear light. Despite these difficulties, and inconsistent with the implication of the early-type host morphologies, an intermediate-age stellar population is present at a significant level. Off-nuclear ($\gtrsim$15 kpc) UV/optical spectra of quasars indicate that old-stellar populations dominate (Hughes et al. 2000; Nolan et al. 2001). However, with much deeper spectra a significant fraction (10% in mass fraction) of an intermediate-age population is revealed (Canalizo et al. 2006; G. Canalizo & A. Stockton 2009, in preparation). In type-2 AGNs and less luminous type-1 objects where the nuclear radiation contamination is less severe, the presence of an intermediate-age stellar population has been extensively confirmed (Kotilainen & Ward 1994; Ronnback et al. 1996; Brotherton et al. 1999; Kauffmann et al. 2003a; Jahnke et al. 2004; Vanden Berk et al. 2006; Jahnke et al. 2007). Furthermore, it seems that there is a decrease in the mean stellar age with increasing AGN luminosity (Kauffmann et al. 2003a; Vanden Berk et al. 2006).

Techniques that are more suitable for detecting ongoing/recent ($\lesssim$ 100 Myr) star formation have been employed recently, although their accuracy is still not comparable to those for normal galaxies. As the material reservoir of star formation, the cold molecular gas mass roughly correlates with the level of star formation. It has been found that quasar hosts are rich in cold molecular gas (Scoville et al. 2003; Evans et al. 2006; Bertram et al. 2007), implying significant ongoing star formation activity. With space-based and AO instruments, spatially resolved images of SFR tracers are promising ways to quantify the SFR and characterize the spatial distribution of the star-forming regions. For example, the extended Paα emission in PG1126-041 is most likely associated with an intense nuclear (100 pc) starburst embedded in the old bulge (Cresci et al. 2004).

A new method to measure the SFR of local quasar hosts is to use the mid-infrared aromatic bands (Ogle et al. 2006; Schweitzer et al. 2006; Shi et al. 2007; Fu & Stockton 2009) measured with the *Spitzer Space Telescope*. In field galaxies, these emission bands are universally bright in roughly solar metallicity regions of star formation, with well understood relationships to the SFR (e.g., Roussel et al. 2001; Dale & Helou 2002; Wu et al. 2005; Brandl et al. 2006; Smith et al. 2007; Engelbracht et al. 2008). Their carriers appear to be destroyed by the harsh radiation fields around high-luminosity AGNs (Genzel et al. 1998; Spoon et al. 2007) and thus any detected aromatic emission is likely from the host galaxy.

In Shi et al. (2007), we provided further evidence for the star formation origin of the aromatic features in quasar hosts: (1) both the overall shape of the aromatic features and the distribution of the 7.7 μm/11.3 μm feature ratio are similar to those in star-forming galaxies; (2) the larger the equivalent widths of the aromatic features, the stronger the far-IR emission in the global SEDs of quasars; (3) quasars lie on the trend of normal galaxies in the plane of the molecular gas mass and the aromatic-derived star formation infrared (SFIR) luminosity. By measuring the aromatic feature fluxes in a large quasar sample (∼200 objects including Palomar-Green (PG), Two Micron All Sky Survey (2MASS) and Third Cambridge Revised Catalog of Radio Sources (3CR)), we obtained a quantitative census of star formation activity in low-redshift quasar hosts (Shi et al. 2007). We showed that quasar hosts have a flatter SFIR luminosity function (LF) than field galaxies, i.e., the quasars lie in very luminous star-forming galaxies more often than would be the case for a random sampling of galaxies without nuclear activity.

As a summary, type-1 quasars at low redshift ($z \lesssim 0.5$) mainly reside in luminous early-type host galaxies but harbor a significant (>10%) fraction of intermediate-age stellar populations and are experiencing intense star formation activity. These properties are rare for normal galaxies, implying that the quasar appears at a special stage of galaxy evolution. In this paper, we probe whether type-1 quasar host galaxies at $z \sim 1$ have similar characteristics.

As demonstrated in our low-redshift work (Shi et al. 2007), the aromatic feature observed with *Spitzer* provides efficient measurements of the SFR in quasar hosts with significantly improved accuracy. To constrain the star formation/quasar interplay at high redshift and to characterize the cosmic evolution of star formation in quasar hosts, we have carried out Infrared Spectrograph (IRS) observations of a complete optically selected type-1 quasar sample (57 objects) at $z \sim 1$ to constrain their SFRs. The sample selection and data reduction are presented in Section 2. The measurement of the aromatic feature flux is discussed in Section 3. We show the results in Section 4 and discuss them in Section 5. The conclusion is presented in Section 6. Throughout the paper, we adopt a cosmology with $H_0 = 70$ km s^{-1} Mpc^{-1}, $\Omega_m = 0.3$, and $\Omega_\Lambda = 0.7$. All magnitudes are defined in the AB magnitude system.

2. SAMPLE AND DATA REDUCTION

Our quasar sample is a subset of the nearly homogeneous parent sample from Richards et al. (2006). The completeness for this parent sample has been well quantified and it has been used to construct the quasar LF. To observe objects in low IR background, we selected all targets at $0.8 \leqslant z \leqslant 1.0$ from the Richards et al. (2006) sample in three fields centered at but significantly larger than three *Spitzer* deep fields, including the *Spitzer* Wide-Area Infrared Extragalactic Survey (SWIRE) ELAIS-N1, SWIRE ELAIS-N2 and SWIRE Lockman Hole. Our three fields have sizes of $15\overset{\circ}{.}85 \times 9\overset{\circ}{.}01$ centered at $16^h11^m00^s$ $+55^\circ00'00''$, $19\overset{\circ}{.}22 \times 12\overset{\circ}{.}0$ centered at $16^h36^m48^s$ $41^\circ01'45''$, and $3\overset{\circ}{.}77 \times 3\overset{\circ}{.}0$ centered at $10^h45^m00^s$ $+58^\circ00'00''$, respectively. Our final sample is composed of 57 Sloan Digital Sky Survey (SDSS) quasars at $0.8 \leqslant z \leqslant 1.0$ and is complete down to SDSS i=19.0. As the SDSS quasar coverage does not fill the above three fields, the effective area is calculated by subdividing the field into small rectangles (about 1 deg^2) and then summing those falling within the actual survey region. This gives an effective area of 88.0 deg^2, which is almost the same as the value (83.0 deg^2) derived from the total effective area of the SDSS-DR3 survey and the relative number of SDSS-DR3 quasars at $0.8 \leqslant z \leqslant 1.0$ included in our sample. Although we observed quasars in low IR background, there are no selection criteria based on the IR fluxes of individual objects.

We obtained IRS spectra of the members of this sample (PI-George Rieke, PID-50196). For objects in the redshift range between 0.8 and 1.0, IRS SL1 (7.4–14.5 μm) covers the 6.2 μm aromatic feature and the spectral range required for continuum subtraction. For objects at $z < 0.9$, the blue wing of the 7.7 μm feature will also be observed if it is present. The IRS staring mode was used for the observations and the exposure time for each object was 240 × 2 s.

The data reduction basically followed the IRS data handbook. Briefly, each basic calibrated data (BCD) image was first cleaned

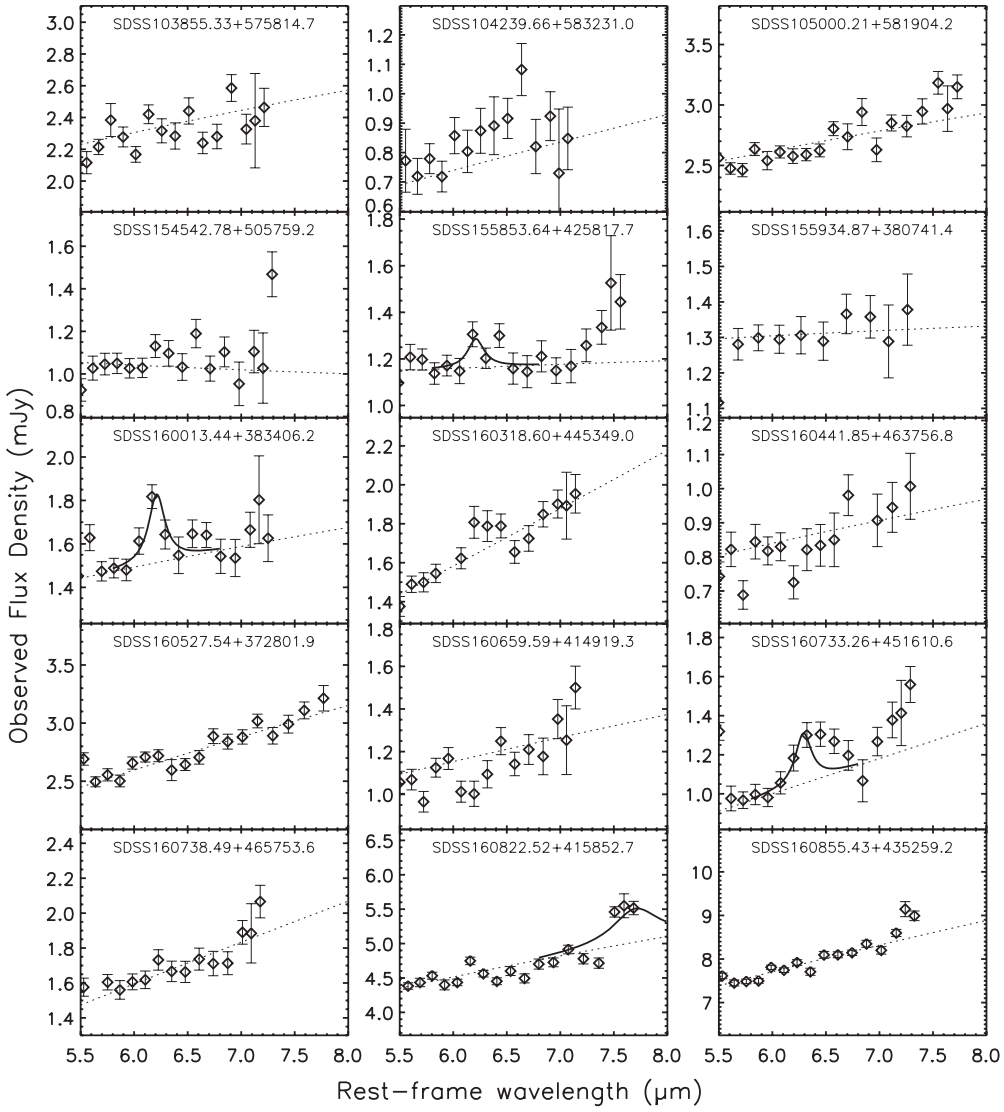

Figure 1. IRS spectra in the rest-frame wavelength (μm) vs. the observed flux density (mJy). The dotted lines show the power-law continua while the solid lines indicate the fitted 6.2 and 7.7 μm features.

using IRSCLEAN. The images observed on the same slit position were sigma-clipped, averaged, and used to subtract the sky for each image observed on another slit position. The spectra were extracted from each sky-subtracted BCD image with the optimal extraction algorithm using SPICE[3] and then sigma-clipped and averaged to produce the final combined spectra. We individually inspected each flux profile along the slit to make sure that the extraction aperture was centered on the brightness peak.

3. MEASUREMENTS OF AROMATIC FEATURES

Because we can work at shorter rest wavelengths, the extraction of the aromatic features is relatively straightforward compared to that for local AGNs in Shi et al. (2007). In that case, careful subtraction of silicate features was needed to measure the 7.7 and 11.3 μm aromatic bands and Monte Carlo simulations were carried out to characterize the measurement uncertainties. In the current situation, for each spectrum the continuum is fitted with a power-law shape to the flux density in the spectral range of 5.8–6.0 μm and 6.8–7.1 μm. We then fitted the continuum-subtracted spectra with two Drude profiles, one centered at 6.22 μm with a FWHM of 0.186 μm and another centered at 7.7 μm with a FWHM of 0.53 μm for the 6.2 μm and 7.7 μm features, respectively (see Smith et al. 2007). For several objects, the central wavelength of the 6.2 μm feature is adjusted between 6.2 and 6.3 μm to achieve the best fit.

The feature flux was obtained by integrating the fitted profile from 1 to 20 μm. For the 7.7 μm feature, the flux was only measured if the rest-frame spectrum wavelength extends longer than 7.4 μm. The noise of the 6.2 μm feature was defined within the spectral range between 6.0 μm and 6.4 μm. For the 7.7 μm feature, the signal-to-noise ratio (S/N) is defined in the spectral range from 7.0 μm to the longest wavelength (usually < 8 μm). Aromatic features with S/Ns above 3 were considered to be solid detections. We inspected each detected feature and excluded several detections due to large noise around the feature. The final detection rate is $\sim$37% for the 6.2 μm feature and $\sim$50% for any feature at either 6.2 or 7.7 μm. The spectra and fitted features are shown in Figure 1. The fluxes or 3σ upper limits are listed in Table 1.

[3] http://ssc.spitzer.caltech.edu/postbcd/spice.html

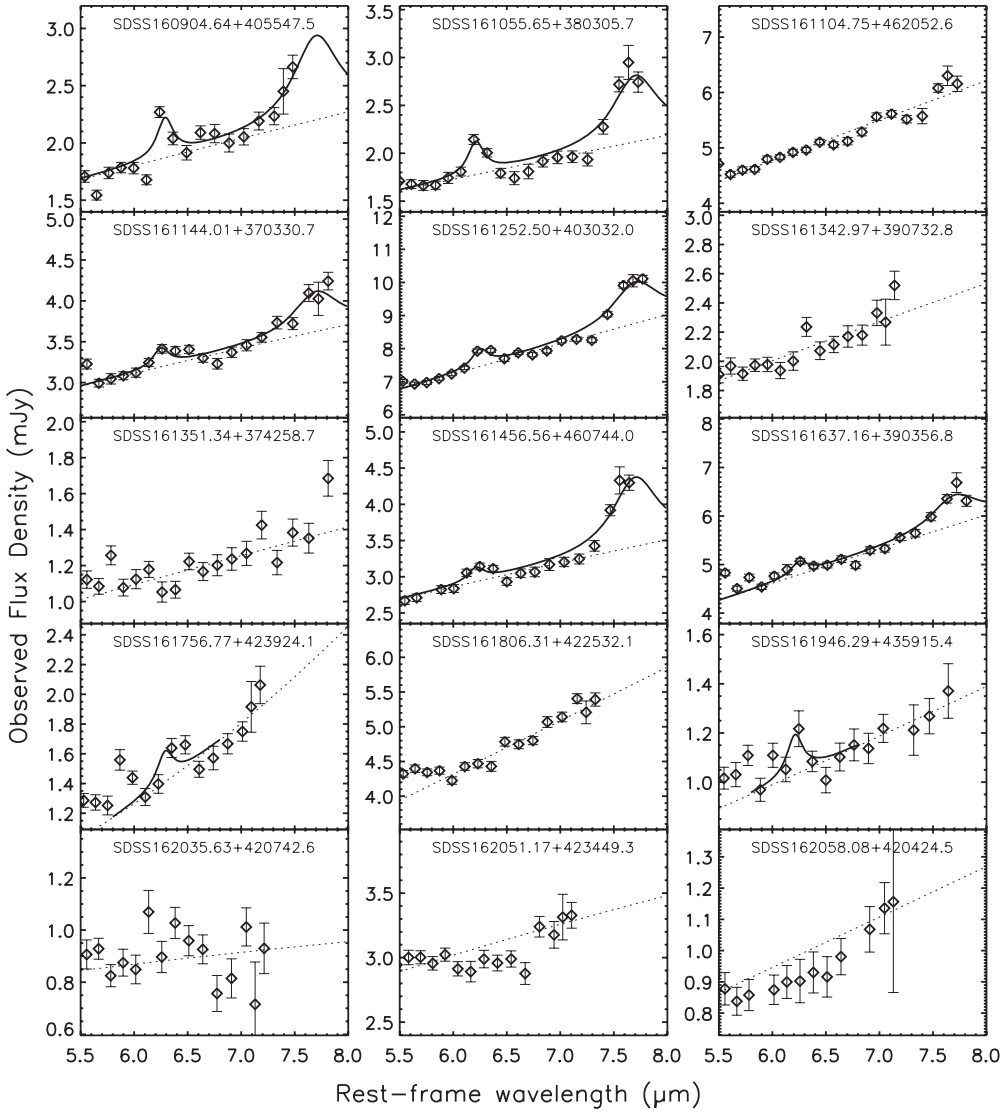

Figure 1. (Continued)

For the 7.7 μm feature, a test based on the four nearby galaxy composite spectra of Smith et al. (2007) shows that a fit only using the blue wing does not introduce a large uncertainty. On the other hand, the silicate emission feature and sometimes the [NeV]7.65 μm line can be present in these type-1 quasars (Shi et al. 2006). To quantify the effect of these two features on the 7.7 μm aromatic fluxes, we have used the above method to measure the feature fluxes in all PG quasars. They are compared to more accurate ones obtained in Shi et al. (2007) by deriving $(f_{7.7\ \mu\mathrm{mPAH}} - f^0_{7.7\ \mu\mathrm{mPAH}})/f^0_{7.7\ \mu\mathrm{mPAH}}$, where $f_{7.7\ \mu\mathrm{mPAH}}$ is the flux based on the method of this paper and $f^0_{7.7\ \mu\mathrm{mPAH}}$ is that derived in Shi et al. (2007). This ratio has an average value of -0.2 and a 68% confidence range from -0.55 to 0.15. The differences are mainly caused by the deviation of the IR spectrum at $\lambda > 8$ μm from the interpolation based on the part below 8 μm. Such a deviation is due to either a change in the IR continuum or the presence of the silicate emission feature. Ten objects out of 57 have both 6.2 and 7.7 μm features and 7 more have detections only of the 7.7 μm feature. The median value of the $f_{7.7\mathrm{PAH}}/f_{6.2\mathrm{PAH}}$ ratio is 4.1 ± 2.4. This ratio is used to obtain the equivalent 6.2 μm feature flux for those objects with only 7.7 μm fluxes.

4. RESULTS

4.1. IR Spectra of $z \sim 1$ Quasars and Comparisons to Other Samples

Shi et al. (2007) found that the profiles and relative strengths of the aromatic features in local AGNs are quite similar to those of local star-forming galaxies, implying star formation excitation of the aromatic features in the AGNs. Figure 2 compares the continuum-subtracted composite spectrum of the whole SDSS sample to those of local galaxies (Smith et al. 2007), local ULIRGs (Rieke et al. 2009), ULIRGs at $z = 1.7$ (Farrah et al. 2008), ULIRGs at $z = 2.8$ (Valiante et al. 2007) and starburst-dominated ULIRGs at $z \sim 2$ from Yan et al. (2007). The composite spectra in the literature were used directly while that of SDSS quasars was derived through the arithmetic mean method (see Shi et al. 2007; Vanden Berk et al. 2001). The continuum of the SDSS composite spectrum is determined by a power-law fit to two spectral regions, 5.9–6.0 and 6.7–6.8 μm. For the comparison, the spectra of other samples were matched to the SDSS one to have the same 6.2 μm aromatic flux. As shown in Figure 2(d), the ULIRGs of Valiante et al. (2007) have a f(7.7 μmPAH)/f(6.2 μmPAH) ratio consistent with that of the

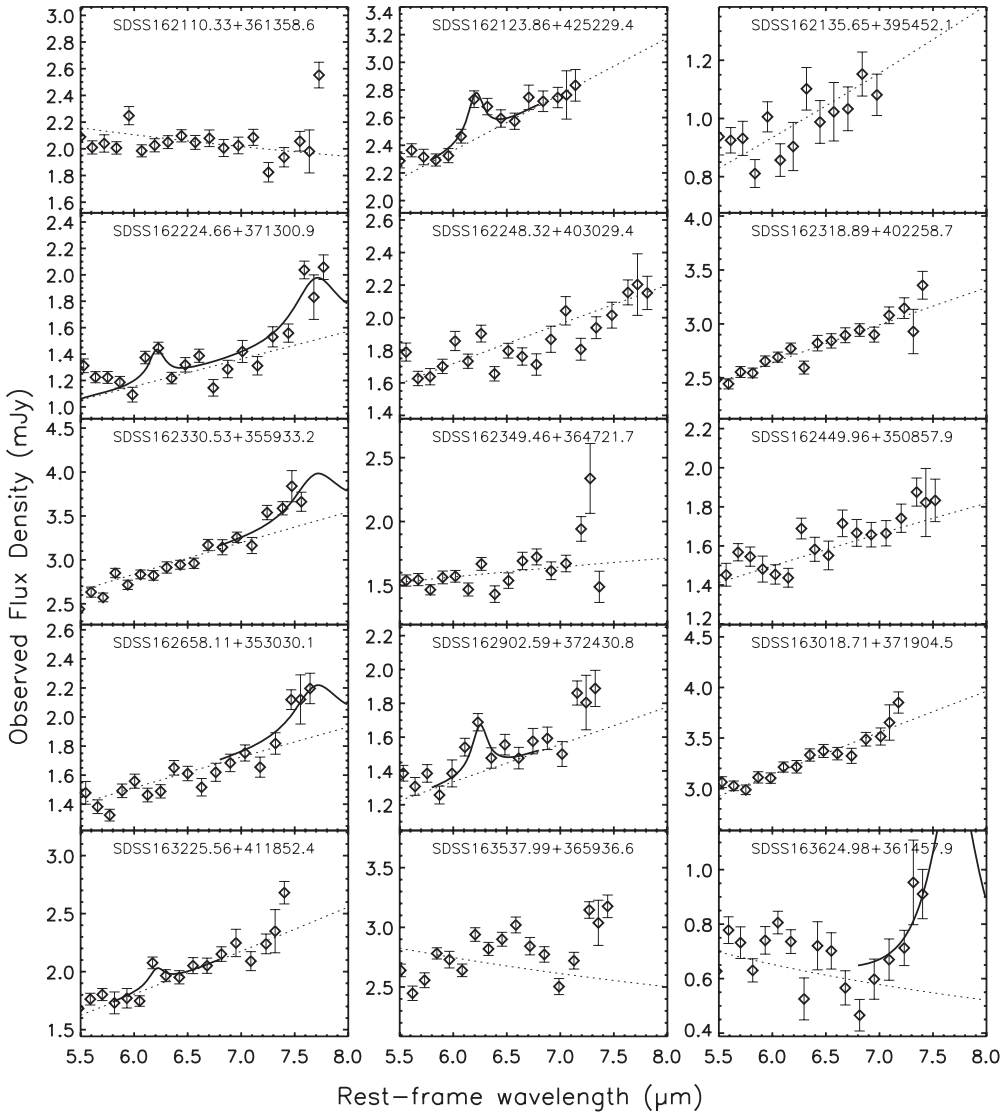

Figure 1. (Continued)

SDSS quasars. A slightly higher flux density around 7.7 μm for the SDSS quasars relative to local galaxies (Figure 2(a)), local ULIRGs (Figure 2(b)) and the ULIRGs of Farrah et al. (2008) (Figure 2(c)) is most likely due to the presence of the emission line [NeV]7.65 μm that is absent in star-formation-dominated galaxies. Only the ULIRGs at $z = 2$ from Yan et al. (2007) have a f(7.7 μmPAH)/f(6.2 μmPAH) ratio significantly different from the SDSS quasar sample. This large deviation is at least partly caused by absorption features around 6 μm, such as water, ice, and hydrocarbons. Therefore, the relative strength of the 6.2 and 7.7 μm aromatic features most likely does not change as a function of redshift or object type. This implies star formation excitation of the aromatic feature in the SDSS quasars.

In Figure 3, we compare the composite spectrum of the whole SDSS sample to those of other quasar samples that are selected with different techniques and at different redshifts. For the comparison, all spectra are normalized by the mean flux density between 5.8 and 6.1 μm. The PG objects are UV/optically selected quasars and thus resemble the SDSS quasars. The comparison between these two samples should provide clues to the redshift evolution of the IR properties in UV/optically selected quasars. Figure 3(a) compares the composite spectrum of the complete SDSS sample to that of the complete PG quasar sample at $z \leqslant 0.5$ from Shi et al. (2007). The power-law slope of the IR continuum is almost the same. The equivalent width (EW) of the 6.2 μm aromatic feature is also similar in the two samples. In the spectral range of the 7.7 μm feature, the SDSS quasars show slightly higher flux density, which may be caused by stronger silicate emission, IR continuum or 7.7 μm feature emission. As shown in Figure 3(b), the sub-sample of the PG quasars used in the QUEST project (Netzer et al. 2007; Schweitzer et al. 2006) shows smaller aromatic feature EWs, which is most likely due to their on average higher nuclear luminosity. To remove the dependence of the aromatic feature EW on the quasar luminosity, we compare the whole SDSS sample to the bright PG sub-sample that is at $M_{\rm B} < -23$ from Shi et al. (2007). The median 5–6 μm continuum luminosity is 7.5×10^{10} and 6×10^{10} $L_{\odot}$ for the SDSS and the bright PG sub-sample, respectively. As shown in Figure 3(c), the bright PG sub-sample has a 7.7 μm feature much weaker than the SDSS quasars while its 6.2 μm feature is relatively noisy but most likely weaker than the SDSS quasars. This indicates that the fraction of the aromatic feature flux in the mid-IR evolves with redshift at a given nuclear luminosity, which can be caused by either higher SFRs in SDSS quasars or the evolution of the aromatic feature with redshift. As shown below, this evolution is

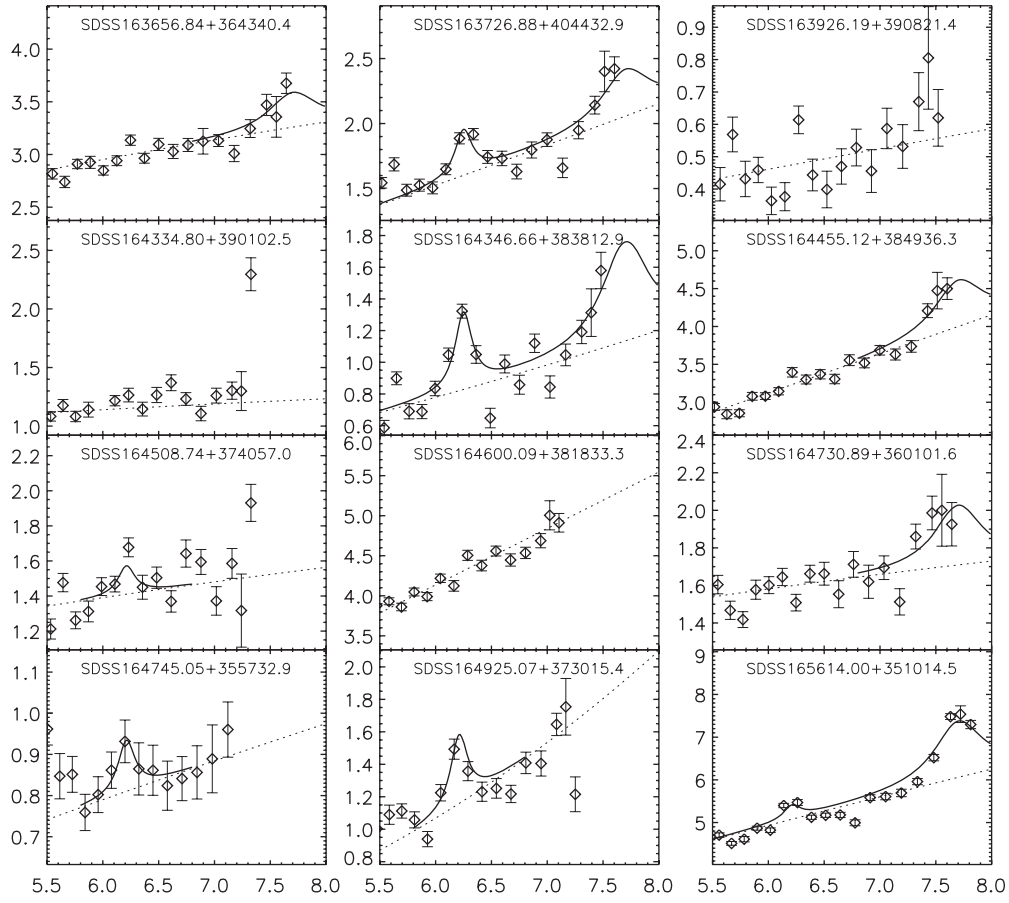

Figure 1. (Continued)

actually dominated by the second effect, i.e., stronger aromatic flux for a given SFR at high redshift.

In Figure 3(d), we compare the SDSS quasars to the mm bright type-1 quasars at $z \sim 2$ from Lutz et al. (2008) that have mid-IR continuum luminosities two orders of magnitude higher than for the SDSS quasars. The IR continuum slope and EWs of the two aromatic features are similar to those of the SDSS quasars. This again suggests that the aromatic feature profile does not change with redshift, luminosity or object type.

The composite spectrum of type-2 QSOs selected in the X-ray from Sturm et al. (2006) is shown in Figure 3(e). This sample spans the redshift range from 0.2 to 1.38 and has a mean redshift of 0.75. The IR continuum is redder than that of the SDSS type-1 quasars. Although no aromatic bands are detected, the spectrum is so noisy that even higher EWs than for the SDSS quasars are still possible. In addition, the median $L_{5-6\,\mu\mathrm{m}}$ of this X-ray-selected sample is about $2.5 \times 10^{11}\ L_{\odot}$, several times higher than that of the SDSS sample. Therefore, in contrast to Sturm et al. (2006), we argue that the S/N of the spectrum is not high enough to rule out the possibility that these X-ray-selected type-2 QSOs have significant star formation activity.

4.2. Star-forming Infrared Luminosity Function of Quasar Hosts at $z = 1$

4.2.1. Conversion Factors from the 6.2 μm Aromatic Flux to the Total Star-forming IR Luminosity

High-redshift star-forming galaxies appear to show evolution in the relative strengths of the total star-forming IR and the aromatic luminosities ($L_{\mathrm{SFIR}}/L_{\mathrm{PAH}}$) (Rigby et al. 2008; Murphy et al. 2009). To convert the aromatic flux of quasar hosts to the corresponding SFR, the ratio ($L_{\mathrm{SFIR}}/L_{\mathrm{PAH}}$) should be defined based on high-redshift star-forming galaxies. A heterogeneous sample of high-redshift star-forming galaxies at $0.5 < z < 1.5$ was compiled from the literature, as listed in Table 2. The object is named by the corresponding reference followed by the name in the reference. The IRS spectra were retrieved from the archive and re-reduced except for Teplitz07-2 for which the published spectrum was used. Since the aromatic fluxes measured with different methods can vary up to several times (Smith et al. 2007), the 6.2 μm features of these star-forming galaxies were measured through the same method as for the quasars. The large equivalent width ($\gtrsim$0.3 μm) of the 6.2 μm feature in these objects indicates the dominant component of the IR radiation is powered by star formation. This is derived from the fact that the composite HII-like star-forming galaxy spectra in Smith et al. (2007) have an EW (6.2 μmPAH) of $\sim$0.3 μm.

To derive the total IR luminosity of these star-forming galaxies, their broadband IR flux densities are fitted with the 14 star-forming templates for the IR luminosity range of $10^{9.75}$–$10^{13} L_{\odot}$ from Rieke et al. (2009). As shown in Table 2, the MIPS 24, 70, and 160 μm photometry is used for the Brand et al. (2008) sample, while IRS 16 μm, MIPS 24 and 70 μm are used for the Murphy et al. (2009) sample. The L_{SFIR}(8–1000 μm) is measured by integrating the template giving the smallest χ^2. For each object, the observed photometry and associated uncertainties are Monte Carlo simulated and re-fitted with the star-forming templates. The standard deviation of the resulting L_{SFIR}(8–1000 μm) is adopted as the 1σ error of L_{SFIR} due to the observed flux uncertainties. An additional error in

Table 1
Aromatic Features in $z \sim 1$ Quasar Hosts

Source	z	m_i	M_g	$F_{6.2\mathrm{PAH}}$ (10^{-15} erg s^{-1} cm^{-2})	$F_{7.7\mathrm{PAH}}$ (10^{-15} erg s^{-1} cm^{-2})	$L_{\mathrm{TIR}}^{\mathrm{SF}}$ (10^{11} $L_\odot$)	$L_{5-6\ \mu\mathrm{m}}$ (10^{11} $L_\odot$)
(1)	(2)	(3)	(4)	(5)	(6)	(7)	(8)
SDSS103855.33+575814.7	0.96	18.56	−24.87	< 2.0		< 3.07	1.19
SDSS104239.66+583231.0	1.00	19.06	−24.44	< 2.2		< 4.24	0.44
SDSS105000.21+581904.2	0.83	17.76	−25.38	< 1.5		< 1.19	1.00
SDSS154542.78+505759.2	0.94	19.04	−24.35	< 1.4		< 1.67	0.52
SDSS155853.64+425817.7	0.87	18.50	−24.75	1.5 ± 0.5		1.43 ± 1.17	0.51
SDSS155934.87+380741.4	0.96	18.39	−25.03	< 1.6		< 2.25	0.54
SDSS160013.44+383406.2	0.95	19.02	−24.39	3.6 ± 0.5		7.12 ± 4.79	0.78
SDSS160318.60+445349.0	0.98	19.05	−24.42	< 2.0		< 3.45	0.71
SDSS160441.85+463756.8	0.94	19.09	−24.30	< 1.3		< 1.56	0.40
SDSS160527.54+372801.9	0.82	17.57	−25.53	< 1.8		< 1.47	1.12
SDSS160659.59+414919.3	0.98	18.97	−24.49	< 1.4		< 2.10	0.57
SDSS160733.26+451610.6	0.94	18.93	−24.47	2.9 ± 0.5		5.04 ± 3.49	0.54
SDSS160738.49+465753.6	0.97	19.06	−24.38	< 1.4		< 1.94	0.97
SDSS160822.52+415852.7	0.84	17.42	−25.74	< 1.4	10.9 ± 2.0	2.92 ± 2.16	1.78
SDSS160855.43+435259.2	0.93	17.25	−26.13	< 1.7		< 2.25	4.23
SDSS160904.64+405547.5	0.89	18.70	−24.58	3.9 ± 0.4	16.0 ± 4.0	6.18 ± 4.21	0.89
SDSS161055.65+380305.7	0.83	18.54	−24.60	4.1 ± 0.4	15.5 ± 1.8	5.26 ± 3.63	0.66
SDSS161104.75+462052.6	0.83	18.80	−24.33	< 1.4		< 1.06	1.82
SDSS161144.01+370330.7	0.81	17.77	−25.31	2.7 ± 0.6	11.2 ± 1.7	2.65 ± 1.99	1.15
SDSS161252.50+403032.0	0.82	17.16	−25.96	6.2 ± 0.5	28.3 ± 1.8	9.16 ± 6.07	3.00
SDSS161342.97+390732.8	0.98	18.25	−25.21	< 1.5		< 2.30	1.07
SDSS161351.34+374258.7	0.81	18.87	−24.21	< 1.6		< 1.23	0.42
SDSS161456.56+460744.0	0.85	18.79	−24.38	2.2 ± 0.5	21.2 ± 2.3	2.28 ± 1.75	1.14
SDSS161637.16+390356.8	0.81	17.89	−25.19	3.2 ± 0.8	14.0 ± 1.7	3.42 ± 2.48	1.72
SDSS161756.77+423924.1	0.97	18.62	−24.84	2.3 ± 0.5		4.08 ± 2.89	0.80
SDSS161806.31+422532.1	0.93	17.94	−25.44	< 1.6		< 2.01	2.40
SDSS161946.29+435915.4	0.85	18.61	−24.58	2.0 ± 0.6		2.01 ± 1.57	0.40
SDSS162035.63+420742.6	0.96	19.08	−24.36	< 1.9		< 2.93	0.48
SDSS162051.17+423449.3	0.99	18.88	−24.61	< 1.7		< 2.79	1.69
SDSS162058.08+420424.5	0.96	18.84	−24.60	< 1.9		< 2.93	0.39
SDSS162110.33+361358.6	0.83	17.88	−25.26	< 1.3		< 0.99	0.79
SDSS162123.86+425229.4	0.98	18.42	−25.04	3.8 ± 0.5		8.44 ± 5.61	1.27
SDSS162135.65+395452.1	0.98	19.05	−24.41	< 1.8		< 2.87	0.50
SDSS162224.66+371300.9	0.82	19.05	−24.05	2.8 ± 0.4	10.6 ± 1.7	2.88 ± 2.13	0.48
SDSS162248.32+403029.4	0.81	18.93	−24.14	< 1.6		< 1.23	0.64
SDSS162318.89+402258.7	0.91	17.78	−25.55	< 1.4		< 1.50	1.20
SDSS162330.53+355933.2	0.87	18.46	−24.76	< 1.5	11.8 ± 3.1	3.72 ± 2.67	1.15
SDSS162349.46+364721.7	0.92	18.49	−24.87	< 1.6		< 1.93	0.72
SDSS162449.96+350857.9	0.88	18.94	−24.32	< 1.6		< 1.69	0.68
SDSS162658.11+353030.1	0.85	18.76	−24.43	< 1.5	7.7 ± 2.1	1.84 ± 1.46	0.55
SDSS162902.59+372430.8	0.93	19.03	−24.34	3.2 ± 0.5		5.60 ± 3.84	0.76
SDSS163018.71+371904.5	0.97	18.39	−25.06	< 1.5		< 2.04	1.84
SDSS163225.56+411852.4	0.91	18.42	−24.91	1.7 ± 0.4		2.07 ± 1.61	0.83
SDSS163537.99+365936.6	0.90	18.35	−24.97	< 1.4		< 1.53	1.26
SDSS163624.98+361457.9	0.91	18.93	−24.40	< 1.5	17.8 ± 4.5	7.92 ± 5.29	0.33
SDSS163656.84+364340.4	0.85	18.54	−24.65	< 1.5	7.4 ± 2.4	1.72 ± 1.38	1.19
SDSS163726.88+404432.9	0.86	18.52	−24.68	4.1 ± 0.4	7.9 ± 2.3	6.03 ± 4.11	0.66
SDSS163926.19+390821.4	0.88	18.88	−24.37	< 1.4		< 1.30	0.21
SDSS164334.80+390102.5	0.93	18.91	−24.45	< 1.6		< 1.97	0.54
SDSS164346.66+383812.9	0.89	18.94	−24.35	5.6 ± 0.4	13.6 ± 3.6	10.50 ± 6.92	0.36
SDSS164455.12+384936.3	0.86	18.78	−24.43	< 1.5	13.5 ± 3.1	4.34 ± 3.06	1.23
SDSS164508.74+374057.0	0.93	19.02	−24.35	1.9 ± 0.5		2.58 ± 1.94	0.73
SDSS164600.09+381833.3	0.99	18.18	−25.30	< 1.5		< 2.36	2.20
SDSS164730.89+360101.6	0.85	18.78	−24.40	< 1.4	7.1 ± 2.3	1.64 ± 1.32	0.63
SDSS164745.05+355732.9	0.94	19.07	−24.33	1.4 ± 0.5		1.81 ± 1.44	0.43
SDSS164925.07+373015.4	0.95	18.97	−24.44	4.9 ± 0.5		10.96 ± 7.21	0.53
SDSS165614.00+351014.5	0.81	17.44	−25.63	3.8 ± 0.6	29.9 ± 1.7	4.37 ± 3.08	1.73
Log $L_{5-6\ \mu\mathrm{m}} \in$ [8.0, 10.8]						$0.18^{+0.09}_{-0.12}$	$0.43^{+0.14}_{-0.23}$
Log $L_{5-6\ \mu\mathrm{m}} \in$ [10.8, 12.5]						$0.25^{+1.22}_{-0.15}$	$1.24^{+2.99}_{-0.60}$

Notes. Column 1: source name; Column 2: redshift; Column 3: the i-band magnitude; Column 4: the rest-frame g-band magnitude; Column 5: the 6.2 μm aromatic feature flux and 3σ upper limits; Column 6: the 7.7 μm aromatic feature flux; Column 7: the aromatic-derived total star-forming IR luminosity; Column 8: the continuum luminosity integrated from 5 to 6 μm. The last two rows are for stacked spectra of individually aromatic-undetected objects within two 5–6 μm luminosity ranges.

Table 2
High-Redshift Star-Forming Galaxies

Sources	z	$F_{16\,\mu m}$ (mJy)	$F_{24\,\mu m}$ (mJy)	$F_{70\,\mu m}$ (mJy)	$F_{160\,\mu m}$ (mJy)	Ref.	$F_{6.2PAH}$ (10^{-14} erg s^{-1} cm^{-2})	EW$_{6.2PAH}$ (μm)	L_{TIR} (10^{11} $L_\odot$)
(1)	(2)	(3)	(4)	(5)	(6)	(7)	(8)	(9)	(10)
Brand08-70bootes3	0.986	...	1.26 ± 0.1	35.0 ± 6.3	145 ± 29	1	0.96 ± 0.07	0.48	46.39
Brand08-70bootes4	0.975	...	1.22 ± 0.1	36.6 ± 5.1	100 ± 20	1	0.84 ± 0.08	0.40	41.29
Brand08-70bootes7	0.664	...	2.18 ± 0.1	51.8 ± 4.7	135 ± 27	1	1.66 ± 0.08	0.51	20.20
Brand08-70bootes9	0.668	...	3.46 ± 0.1	67.2 ± 3.1	245 ± 49	1	3.29 ± 0.12	0.79	29.68
Murphy09-ID3	0.63	0.774 ± 0.006	1.210 ± 0.005	11.1 ± 0.53	...	2	1.18 ± 0.03	0.72	6.60
Murphy09-ID8	0.64	0.399 ± 0.006	0.721 ± 0.005	11.1 ± 0.53	...	2	0.56 ± 0.02	0.49	4.93
Murphy09-ID11	1.22	0.993 ± 0.006	0.446 ± 0.005	13.2 ± 0.53	...	2	0.76 ± 0.03	0.73	53.28
Murphy09-ID22	0.64	0.580 ± 0.006	0.750 ± 0.005	5.53 ± 0.53	...	2	0.89 ± 0.03	0.58	4.16
Teplitz07-2	1.09	...	0.133 ± 0.015	...	...	3	0.16 ± 0.03	0.70	3.82

Note.
References. (1) Brand et al. 2008; (2) Murphy et al. 2009; (3) Teplitz et al. 2007.

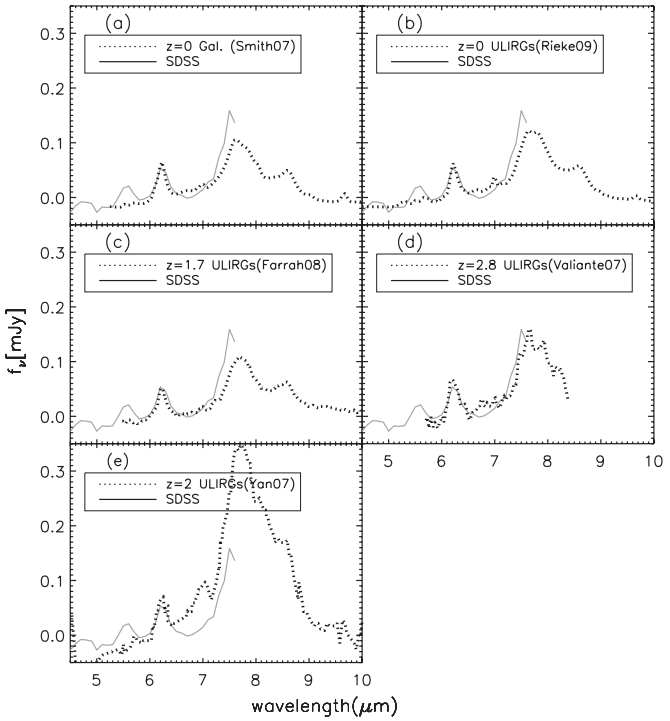

Figure 2. Continuum-subtracted composite spectrum of the whole SDSS sample (solid lines) compared to those (dotted lines) of local galaxies (Smith et al. 2007), local ULIRGs (Rieke et al. 2009), ULIRGs at $z = 1.7$ (Farrah et al. 2008), ULIRGs at $z = 2.8$ (Valiante et al. 2007), and starburst-dominated ULIRGs at $z \sim 2$ from Yan et al. (2007).

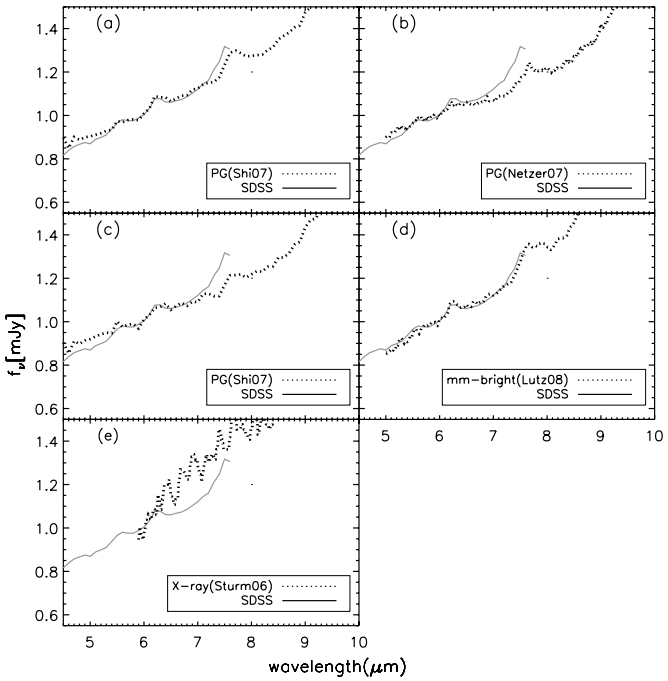

Figure 3. Composite spectrum (solid lines) of the whole SDSS sample compared to those of other quasar samples (dotted lines).

L_{SFIR} due to the scatter of the template itself is estimated as $(L_{SFIR}^{templatei+1} - L_{SFIR}^{templatei-1})/2$, where the template i is the one giving the minimum χ^2. The two errors are added quadratically to give the final error in L_{SFIR}. Murphy et al. (2009) have shown that the L_{SFIR} using photometry including MIPS 70 or 160 μm flux densities is an unbiased estimate of the total IR luminosity based on photometry from the near-IR to the submillimeter. For one object (Teplitz07-2) with only 24 μm data, its 24 μm flux density is converted to the total IR luminosity using the redshift-dependent $L_{24\,\mu m}$–L_{SFIR} relationship and the 1σ scatter is assumed to be 0.2 dex (Rieke et al. 2009). Murphy et al. (2009) show that, at $z \sim 1$, the total IR luminosity estimated from the MIPS 24 μm flux density does not suffer from any systematic shift because the aromatic flux contributes a small fraction at rest-frame 12 μm.

Figure 4 shows the L_{SFIR} versus L_{PAH} for these high-redshift star-forming galaxies. As a comparison, the local relationship is shown as the dash-dotted line based on the star-forming template of Rieke et al. (2009). There is a factor of 2–3 decrease in the $L_{SFIR}/L_{6.2PAH}$ at $z \sim 1$ compared to the local behavior. We used the IDL code linmix_err.pro (Kelly 2007) that employs a Bayesian approach to perform linear regression of two variables with measured errors. The following relationship is derived for quasar hosts at $z \sim 1$:

$$\log(L_{SFIR}) = (12.16 \pm 0.09) + (1.42 \pm 0.29)(\log(L_{6.2PAH}) - 9.85) \pm 0.25. \quad (1)$$

Note that the relationship is obtained between $\log(L_{SFIR})$ and $L_{6.2PAH} - \langle L_{6.2PAH} \rangle$. In this case, the slope and intercept of the relationship are independent of each other. The median and 1σ range of the regression line are shown as solid and dotted lines, respectively, in Figure 4. As shown in Table 2, we do not have

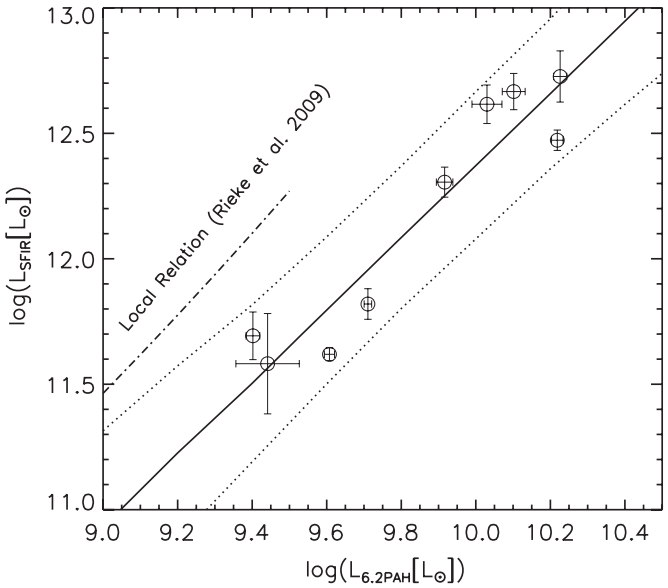

Figure 4. $L_{\rm SFIR}$ vs. $L_{6.2\,\mu{\rm mPAH}}$ for high-redshift star-forming galaxies as listed in Table 2. The solid line and dotted line show the linear regression fit to the data and the associated scatter, respectively. The dot-dashed line shows the local relationship based on the star formation template of Rieke et al. (2009).

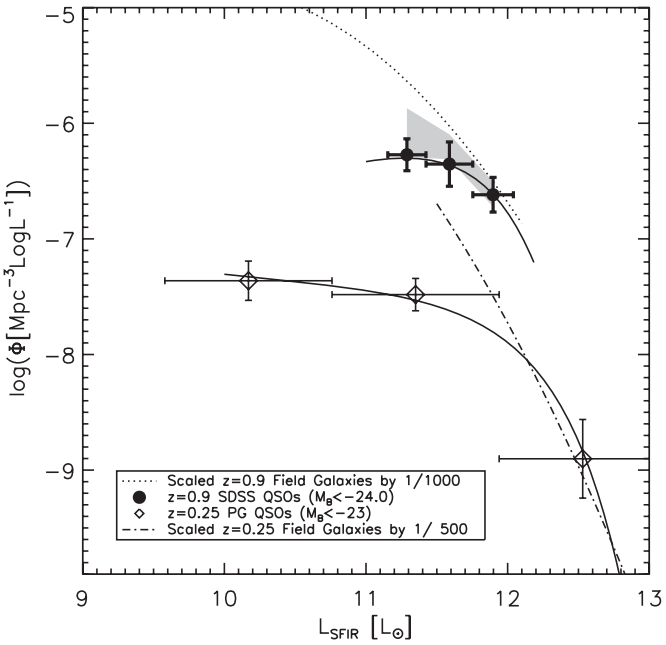

Figure 5. Star-forming IR luminosity function (SFIR LF) of $z \sim 1$ quasar hosts (filled circles) compared to that of low-redshift PG quasars (open diamonds). The gray area shows the 1σ range of the SFIR LF after correcting the effect due to the uncertainty of the SFIR luminosity (see the text for details). The SFIR LFs of field galaxies at both low and high redshifts are also shown for comparison.

star-forming galaxies at $z \sim 1$ with total IR luminosities below $10^{11}\,L_{\odot}$. It thus may be invalid to extrapolate this relation below $10^{11}\,L_{\odot}$.

As our objects have LIRG-level SFIR luminosities, the conversion factor $L_{\rm SFIR}/L_{\rm PAH}$ is about three times lower compared to the local relationship. Therefore, our estimate of evolution of star formation in quasar hosts is conservative. If we adopt the local relationship for our $z \sim 1$ quasars, as some works provide tentative evidence for no evolution in $L_{\rm SFIR}/L_{\rm PAH}$ ratio (e.g., Magnelli et al. 2009), then the evolution from $z \sim 1$ to $z \sim 0$ would be increased by a factor of about three above our estimate.

4.2.2. Star-forming IR Luminosity Function of $z \sim 1$ Type-1 Quasars

The SFIR LF of the $z \sim 1$ type-1 quasar hosts is constructed by counting the number of objects in different luminosity bins and redshift bins ($\Delta L \Delta z$). For this method, in the lowest luminosity bin that intersects the flux limit at a given redshift, only part of the $\Delta L \Delta z$ space above the flux limit can be filled by objects. To account for this partly filled bin, we have used a revised $1/V_{\rm max}$ method (Page & Carrera 2000) to derive the LF. The incompleteness function for the quasar selection is given by Richards et al. (2006). The luminosity bins are defined to have roughly the same number of objects and range from the lowest observed luminosity to the highest one.

Figure 5 shows the SFIR LF of $z \sim 1$ type-1 quasar hosts compared to the LF of contemporary field galaxies from Le Floc'h et al. (2005) and to that of the $z = 0.25$ PG quasars. The SFIR LF of the PG quasars has been updated by using the $L_{\rm SFIR}/L_{\rm PAH}$ ratio of Rieke et al. (2009), but there is only a small change. The error bar shows the Poisson uncertainty. The uncertainty in the SFIR luminosity can smooth the LF by scattering more objects out of the luminosity bin originally with a larger number of objects. To quantify this effect, a set of 1000 SFIR LFs were Monte Carlo simulated using the observed $L_{\rm SFIR}$ and associated uncertainties. The relative change in the number density for each luminosity bin is then quantified. The gray area then shows the 1σ range of the SFIR LF after correcting for the effects due to the uncertainty of the SFIR luminosity.

Shi et al. (2007) carried out a series of simulations to demonstrate that the PG quasars have a flat SFIR LF compared to that of field galaxies. As shown in the figure, such a trend most likely exists at $z \sim 1$. Within our limited range of luminosity, the difference between the $z \sim 0.25$ and $z \sim 1$ SFIR LFs can be described as pure density evolution.

4.2.3. Cosmic Evolution of the Comoving SFIR Luminosity Density and Average SFR in Quasar Hosts

With the SFIR LF at $z \sim 0.25$ and $z \sim 1$, we now can quantify the cosmic evolution of the comoving SFIR luminosity density in type-1 quasar hosts. Due to the lack of constraints on the slope at low luminosity, two types of estimation have been explored. First, we can estimate the comoving SFIR density by simply integrating the available data points, which gives an evolution factor of 10 ± 4. Second, we can fit the SFIR LF with a series of Schechter functions whose slopes (α) are Monte Carlo simulated. For the PG sample, the slopes are simulated using the number densities and associated uncertainties in two low-luminosity bins. For the SDSS sample, as the slopes given in a similar way have large uncertainties, we attempt to use the objects with undetected aromatic features to constrain the slope α. Basically, for a range of assumed slopes, we fitted data points to obtain a series of analytic Schechter LFs. For each LF, a SFIR luminosity is then randomly assigned to a SDSS quasar with the relative probability following that of the LF. The detection rate of the aromatic feature is then calculated by comparing the simulated SFIR luminosity to the observed 3σ uncertainty of the SFIR luminosity. Figure 6 shows the simulated aromatic detection rates (points) compared to the observed one (lines). The derived slope is $\alpha = -0.59 \pm 0.25$. By Monte Carlo simulating this slope, the observed LF is fitted with a series of Schechter functions, which is shown as a solid line in Figure 5 and listed in Table 3. We obtained $\log L^* = 11.64 \pm 0.19$. The comoving SFIR luminosity density is then obtained

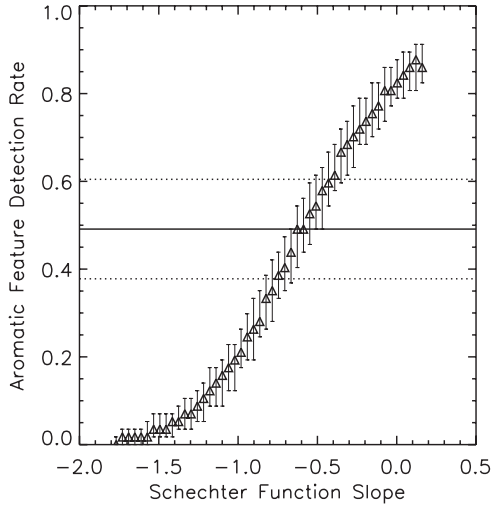

Figure 6. Triangles show the predicted detection rate of the aromatic feature of the SDSS sample for a range of the assumed Schechter function slope. The solid line is the observed detection rate while the associated uncertainty is shown as the dotted line.

Table 3
Best-Fitting Parameters to Star-forming IR LF of SDSS and PG Quasars

Object	$\log(\phi^\star$ (Mpc^{-3} log $L^{-1}))$	$\log(L^\star$ $(L_\odot))$	α
SDSS	-6.30 ± 0.16	11.64 ± 0.19	-0.59 ± 0.25
PG(M_B <−23)	-7.86 ± 0.39	12.04 ± 0.34	-1.10 ± 0.19

Notes. The slope for the SDSS sample is derived by producing the observed aromatic detection rate (see Figure. 6), while the one for the PG sample is calculated using the number densities and associate uncertainties in two low-luminosity bins. By Monte Carlo simulating the derived slope, ϕ^* and L^* are obtained by fitting Schechter functions to the observed LFs. All uncertainties are given at the 1σ level.

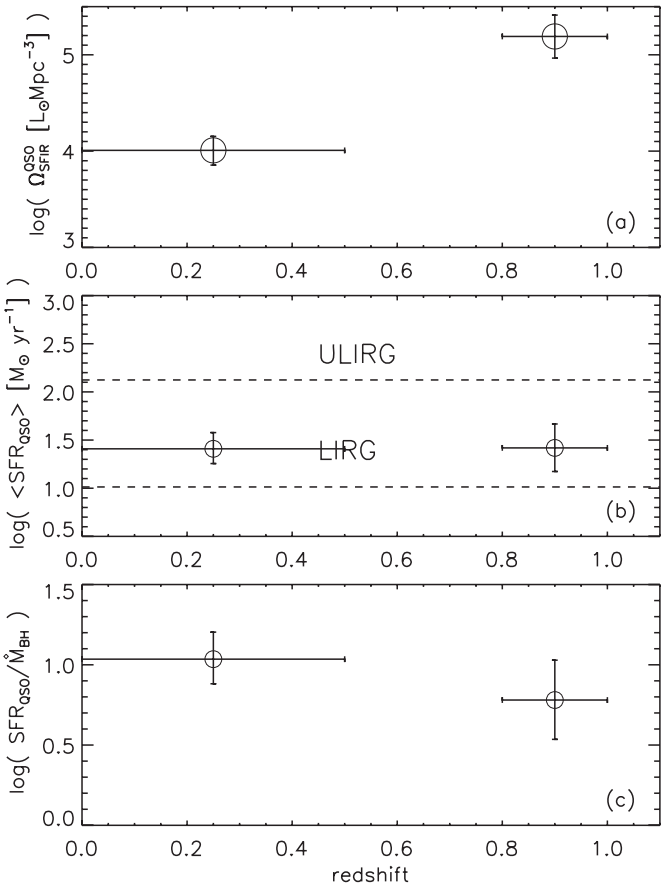

Figure 7. Cosmic evolution of the comoving SFIR luminosity density (a), the average SFR (b) and the average SFR/$\dot{M}_{\rm acc}$ (c) in type-1 quasar hosts. The SFIR luminosity is converted to the SFR using Rieke et al. (2009) relations that deviate from those of Kennicutt (1998) by a factor of ∼1.5 as a result of a different initial mass function.

by integrating the fitted Schechter functions and the result is shown in Figure 7(a). In this method, the derived increase of the comoving SFIR luminosity density in quasar hosts from $z = 0.25$ to $z = 0.9$ is 15^{+7}_{-5} (1σ). In either case, the SFIR energy density in type-1 quasar hosts shows a dramatic evolution, much larger than the behavior of the general field galaxies (which increase by a factor of $5^{+1}_{-0.7}$; Le Floc'h et al. 2005; Pérez-González et al. 2005).

The integration of the LF is carried out in the luminosity range $[10^{10}, 10^{12}]$ $L_\odot$. If we vary the upper or lower limits by a factor of 10, the derived evolution changes little. If we had used the local conversion of the aromatic luminosity to the SFR, the evolution of the quasar host SFRs would roughly triple.

We now consider how selection biases might influence this result. We quantified the evolution of the comoving SFIR luminosity density in quasar hosts by measuring the SFR in PG quasars and SDSS quasars, two samples selected through different UV/optical criteria. The SDSS quasars were selected on the basis of multiple color-color diagrams (Richards et al. 2001); nonetheless, as with the PG sample, UV excess is the dominant characteristic. The incompleteness of the PG quasar selection ($U - B < -0.46$ and $B < 16.16$) has long been known (Goldschmidt et al. 1992; Wisotzki et al. 2000; Mickaelian et al. 2001; Jester et al. 2005). Comparisons of PG quasars to other quasar surveys indicate a completeness of ∼50%–100% (Wisotzki et al. 2000; Mickaelian et al. 2001; Jester et al. 2005). The incompleteness is most likely independent of the quasar optical and radio properties within the PG quasar selection criterion itself (Jester et al. 2005), i.e., PG quasars are representative of quasars that are bright at B band. Therefore, the evolution of the comoving SFIR luminosity density in type-1 quasar hosts is overestimated at most by a factor of 2. In addition, our $z \sim 1$ quasars ($M_i < -24.7$; $M_B <\sim -24.0$) are brighter than our low-redshift PG quasars by one magnitude ($M_B < -23$). Our study of PG quasars showed that brighter PG quasars have a flatter SFIR LF, implying on average a stronger SFR in a brighter PG quasar host. However, the integral SFIR density is actually lower by a factor of 2 for PG quasars at $M_B < -23$ compared to the value for $M_B < -22$, simply due to lower number densities. The evolution of the comoving SFIR density in quasar hosts may be even larger if we compare quasars at the same brightness cut. Therefore, the two factors (incompleteness of the PG sample and unmatched brightness limit of two quasar samples) tend to cancel each other out. We conclude that the evolution of the comoving SFIR luminosity density in type-1 quasar hosts is indeed much larger than that in field galaxies.

We can use the SFIR LF of quasar hosts to derive the average SFR per object:

$$\langle \mathrm{SFR_{qso}} \rangle = \frac{\int_0^\infty \mathrm{SFR}_{L_{\rm SFIR}} \Phi_{\rm SFIR} dL_{\rm SFIR}}{\int_{L^{\rm limit}_{\rm qso}}^\infty \Phi_{\rm qso} dL_{\rm qso}}, \quad (2)$$

where $\Phi_{\rm SFIR}$ is the SFIR LF of quasar hosts and $\Phi_{\rm qso}$ is the LF of the quasar luminosity at the wavelength where the

quasar sample is selected. The result is shown in Figure 7(b), where $L_{\rm SFIR}$ is converted to the SFR using the relation SFR($M_\odot$ yr^{-1}) $= 6.37 \times 10^{-12}\,(L_{\rm TIR}/L_\odot)^{1.11}$ at $L_{\rm TIR} > 10^{11}\,L_\odot$ and SFR($M_\odot$ yr^{-1}) $= 2.31 \times 10^{-11}\,(L_{\rm TIR}/L_\odot)^{1.06}$ at $L_{\rm TIR} \leqslant 10^{11} L_\odot$ (Rieke et al. 2009). These relationships deviate from those of Kennicutt (1998) mainly due to a different initial mass function. As shown in Figure 7(b), the average SFR in the quasar host is the LIRG level (and remains in the LIRG range with the local $L_{\rm SFIR}/L_{\rm PAH}$ applied at $z \sim 1$). The evolution of this average SFR is very insignificant, and remains small even with application of the local $L_{\rm SFIR}/L_{\rm PAH}$ at $z \sim 1$. As we noted above, our SDSS quasar sample is limited at a magnitude ($M_B < -24$) brighter than the PG quasar limit ($M_B < -23$). Brighter quasars have on average higher SFRs (Shi et al. 2007). PG quasars at $M_B < -23$ have SFRs on average a factor of 1.3 higher than PG quasars at $M_B < -22$. Therefore, the average SFR in the optical type-1 quasar is most likely nearly constant with redshift. This result supports our conclusion that most of the host galaxy SFIR LF evolution is in density, not in luminosity. Here we simply assume that the same SFR–$M_{\rm B}$ trend holds at $z = 0$ and $z = 1$ and that the trend between $M_B = -22$ to -23 holds up to $M_B = -24$, which is most likely true based on the correlation between SFR and quasar nuclear luminosity as discussed in Section 4.3. Note that the three derived quantities in Figure 7 do not depend on the integration limit. For example, the change is only about 0.1 dex using the observed range of the SDSS sample ([10^{11}, 10^{12}]).

4.3. The SFIR Luminosity as a Function of Quasar Nuclear Luminosity

The SFIR LF of the type-1 quasar hosts gives a global sense of their star-forming activity. The enhanced SFR in the quasar hosts as implied by the SFIR LF indicates that further investigation of the star formation activity in individual objects is critical to understand the interplay between star formation and nuclear activity. As shown in Shi et al. (2007), the brighter PG quasars have on average higher SFRs as measured from their SFIR LF. We now search for direct correlations between the SFIR luminosity and quasar nuclear luminosity.

Figure 8 shows the result for the whole PG sample of 90 objects (triangles) and the whole SDSS sample of 57 objects (stars). As there is no significant redshift evolution of the SFRs in the quasar hosts (Section 4.2.3), the two quasar samples are plotted together. The 5–6 μm IR continuum luminosity ($L^{\rm NUC}_{5-6\,\mu{\rm m}}$) is used as a tracer of nuclear luminosity. For clarity, the uncertainty of the SFIR luminosity ($L_{\rm SFIR}$) is not shown in the figure. A significant number (50%) of objects only have upper limits. To demonstrate there is a correlation between the SFIR luminosity ($L_{\rm SFIR}$) and nuclear luminosity, we stacked spectra of several sub-samples of quasars without aromatic detections defined within certain $L^{\rm NUC}_{5-6\,\mu{\rm m}}$ luminosity bins. The result is shown in Figure 9. Each composite spectrum has detected aromatic features. The 6.2 μm feature is measured as in this paper while the 7.7 and 11.3 μm features are measured following Shi et al. (2007). For each sub-sample, the mean $L^{\rm NUC}_{5-6\,\mu{\rm m}}$ is used and the corresponding SFIR luminosity is measured based on the composite spectrum. The result is shown as large symbols in Figure 8. The $L^{\rm NUC}_{5-6\,\mu{\rm m}}$ range of each sub-sample is used as the uncertainty of the $L^{\rm NUC}_{5-6\,\mu{\rm m}}$, and the corresponding $L_{\rm SFIR}$ range is used as the uncertainty of the $L_{\rm SFIR}$.

To quantify the correlation, linear regression fits were carried out using linmix_err.pro that accounts for the measured errors and upper limits. We performed fits to three data sets: all

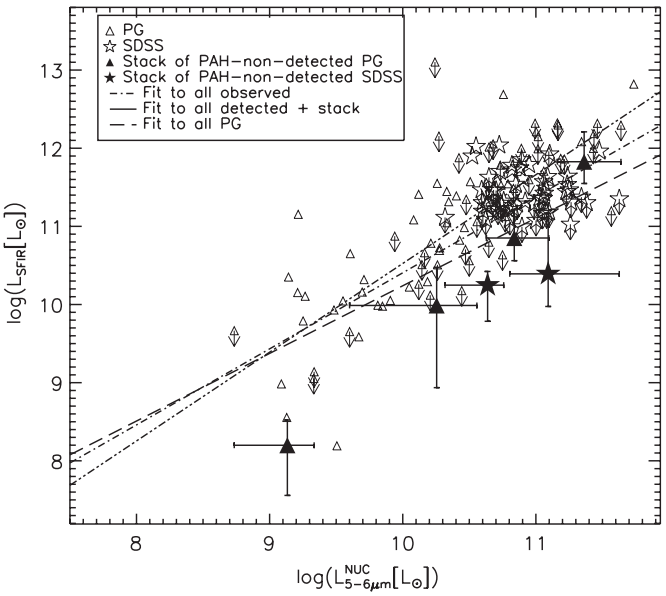

Figure 8. Correlation between the star-forming IR luminosity and the nuclear luminosity at 5–6 μm. The open triangles and stars are for individual PG and SDSS quasars, respectively. The large filled symbols show the result based on the composite spectra of aromatic-undetected objects within 5–6 μm luminosity ranges as indicated by their error-bars on the X-axis (see Figure 9). Three linear regression fits are listed in Table 4.

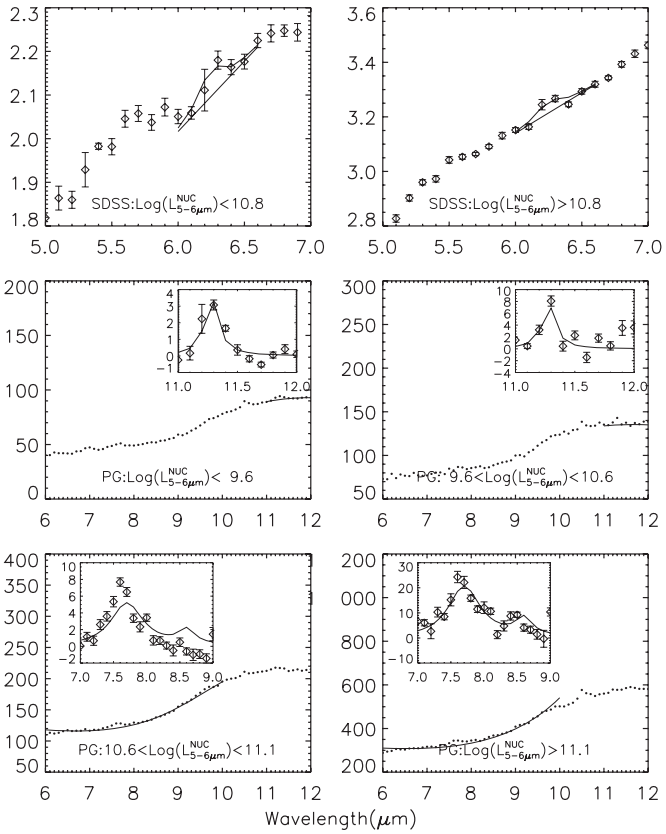

Figure 9. Composite spectra of PG and SDSS quasars without aromatic detection within given 5–6 μm luminosity ranges.

individual PG+SDSS data points, all detected + stacked data points and all PG objects. The best-fit lines are shown in Figure 8 and listed in Table 4. As shown in the figure, the three fits give roughly similar results and have correlation coefficients of 0.6–0.8. Such consistent results confirm the existence of the

Table 4
Best-Fitting Parameters to the Correlation $L_{\rm SFIR}$–$L^{\rm NUC}_{5-6\,\mu{\rm m}}$

Data Set	Best-fitting Formula	Correlation Coefficient
All PG + SDSS	$\log(L_{\rm SFIR}) = (10.98 \pm 0.05) + (0.97 \pm 0.08)(\mathrm{Log}(L_{5-6\,\mu{\rm m}}) - 10.58) \pm 0.52$	0.76 ± 0.05
All detected plus stacked points	$\log(L_{\rm SFIR}) = (11.00 \pm 0.07) + (1.14 \pm 0.11)(\mathrm{Log}(L_{5-6\,\mu{\rm m}}) - 10.42) \pm 0.56$	0.81 ± 0.05
All PG	$\log(L_{\rm SFIR}) = (10.54 \pm 0.12) + (0.86 \pm 0.15)(\mathrm{Log}(L_{5-6\,\mu{\rm m}}) - 10.37) \pm 0.75$	0.64 ± 0.11

Notes. The correlations are derived between $\log(L_{\rm SFIR})$ and $\log L^{\rm NUC}_{5-6\,\mu{\rm m}} - \mathrm{mean}(L^{\rm NUC}_{5-6\,\mu{\rm m}})$. In this case, the uncertainties of the intercept and slope are independent.

correlation and the lack of systematic difference between $z = 1$ SDSS and low-redshift PG samples.

To further demonstrate that the correlation is not caused by the aromatic feature nondetections in about half the objects, we carried out a Monte Carlo simulation for the PG sample, which spans a large range of SFIR luminosity. Basically, a SFIR luminosity is assigned randomly to a PG quasar with the relative probability following the SFIR LF of the whole PG sample. In such a simulation, the SFIR luminosity is assumed not to correlate with the nuclear luminosity. For each set of simulations, a sub-sample of objects with aromatic detections can be defined through comparing the simulated $L_{\rm SFIR}$ and the observed uncertainties or upper limits. The Spearman's correlation coefficient can be measured for the $\mathrm{Log}(L_{\rm SFIR})$–$\mathrm{Log}(L^{\rm NUC}_{5-6\,\mu{\rm m}})$ of such a sub-sample. After 10,000 simulations, the probability of the simulated Spearman's correlation coefficients being higher than the observed one is only 1%.

Both of these tests imply that the SFIR luminosity most likely correlates with the nuclear luminosity in type-1 quasar hosts. The comparison of this correlation to those in theoretical models is presented in Section 5.3.

5. DISCUSSION

5.1. Comparison with Other Studies of AGNs at High Redshift

Intense star formation in high-redshift quasars has been observed in some individual quasars as indicated by rest-frame far-IR emission (e.g., Wang et al. 2008), aromatic features (Lutz et al. 2008), molecular gas emission (for a review, see Solomon & Vanden Bout 2005) and UV emission (Akiyama 2005). However, these studies suffer from low number statistics, selection bias toward high SFRs and large uncertainties in the derived SFR. Hatziminaoglou et al. (2008) have studied IR SEDs of SDSS quasars in the SWIRE field through fitting torus models and star formation templates. They derived on average star formation contributions of ∼35% to the total IR luminosity for quasars at $z = 0.8$–1.0, corresponding to a SFIR luminosity of $\sim 10^{12} L_{\odot}$. However, this high SFR is only for objects detected at MIPS 70 and/or 160 μm, indicating a bias toward high SFRs in their sample. Our study of a complete sample of 57 SDSS quasars demonstrates conclusively that type-1 quasars reside in host galaxies with intense star formation. As the nucleus is brighter due to selection effects and the host galaxy is apparently smaller and fainter due to surface-brightness dimming, the host morphologies are difficult to constrain unambiguously (for a review, see Davies 2008) but appear to be consistent with elliptical morphologies (Kukula et al. 2001; Hyvönen et al. 2007; Falomo et al. 2004; Kotilainen et al. 2007; Falomo et al. 2008; Ammons et al. 2009). We will discuss this apparent inconsistency between early-type host morphology and intense star formation in Section 5.2.1.

Similar to their low-redshift counterparts, IR-selected type-2 quasars largely show disturbed morphologies (Lacy et al. 2007; Urrutia et al. 2008) and have intense star formation activity as probed by the aromatic feature (Lacy et al. 2007; Hernán-Caballero et al. 2009). High SFRs are also found for optically selected type-2 quasars, based on the aromatic feature (Zakamska et al. 2008). High-z ULIRGs with embedded AGNs (possibly related to type-2 quasars) have also been found to be associated with intense star formation (e.g., Houck et al. 2005; Weedman et al. 2006; Yan et al. 2007; Sajina et al. 2007; Watabe et al. 2009).

A correlation between the mean stellar population age and the AGN luminosity is found for high-redshift X-ray-selected AGNs (Ammons et al. 2009). Although some studies do not confirm strong ongoing SFRs in X-ray-selected AGNs with a range of the X-ray luminosity (Sturm et al. 2006; Alonso-Herrero et al. 2008; Schawinski et al. 2009), a more thorough investigation of star formation in a relatively large sample with more plausible probes should be made before concluding that the X-ray-selected AGNs are in a different evolutionary stage. For example, a recent study of X-ray-selected AGNs in the COSMOS field indicates enhanced SFRs in their host galaxies relative to field galaxies with similar stellar masses (Silverman et al. 2009). It also suggests that a selection bias may account for the X-ray-selected AGNs residing in the green valley region of the color-magnitude plot.

To summarize, AGNs at high redshift ($z > 0.5$), including high-luminosity type-1/type-2 quasars and relatively low-luminosity X-ray-selected AGNs, are experiencing intense star-forming activity in their host galaxies.

5.2. Quasar Host Galaxies as a SFR-enhanced Subset of Field Galaxies

We have measured the aromatic-based SFR for a complete sample of SDSS type-1 quasars at $z \sim 1$. The derived SFIR LF is flatter than that of $z \sim 1$ field galaxies, implying enhanced SFRs in the quasar hosts. Combining this with studies of IR- and optically selected type-2 quasars (Lacy et al. 2007; Zakamska et al. 2008; Hernán-Caballero et al. 2009), we conclude that the quasar host galaxy population is a SFR-enhanced subset of field galaxies. This has been known to be true for low-redshift quasars as shown in our study of local optically selected PG, IR-selected 2MASS, and radio-selected 3CR quasars (Shi et al. 2007).

As discussed in the introduction, there are many different ways to probe the stellar population age. To interpret results with different probes, one must keep in mind that each probe is only sensitive to stellar populations with certain ranges of ages and suffers from different limitations. Therefore, apparently different results about the stellar population age of quasar hosts by different studies are not necessarily inconsistent with each other, but instead should be integrated to achieve the complete view of the stellar population that is critical to understand the BH/galaxy co-evolution. In the following, we reconcile our result of enhanced SFRs with different results in the literature.

5.2.1. Comparisons with Host Galaxy Morphology Studies

The IR- and optically selected type-2 quasar hosts show high merger (>50%) fractions at both low (Canalizo & Stockton 2001; Hutchings et al. 2003; Marble et al. 2003) and high redshift (Lacy et al. 2007; Urrutia et al. 2008; Hernán-Caballero et al. 2009), higher than field galaxies of similar infrared luminosity (∼30%; Shi et al. 2009; Sobral et al. 2009). The enhanced SFR in type-2 quasars is thus consistent with their host morphologies.

For optically/UV-selected type-1 quasar hosts, regular early-type morphologies dominate, with a fraction of >50% for quasars at $M_B < -23$ at low redshift ($z < 0.5$; Hutchings et al. 1984; Smith et al. 1986; McLeod & Rieke 1995; Bahcall et al. 1997; Dunlop et al. 2003; Floyd et al. 2004; Guyon et al. 2006). At high redshift, the host galaxies appear to be consistent with elliptical morphologies (Kukula et al. 2001; Hyvönen et al. 2007; Falomo et al. 2004; Kotilainen et al. 2007; Falomo et al. 2008; Ammons et al. 2009), despite the difficulties in constraining the types unambiguously. The merger fraction is <30%, not significantly different from field galaxies. Therefore, the enhanced SFR in the type-1 quasar hosts is not a natural result of the fact that the host galaxy is massive, given the dominance of regular early-type morphologies.

To reconcile the apparent inconsistency between elliptical-dominated morphologies and enhanced SFRs, we propose that star formation in type-1 quasar hosts occurs in the circumnuclear (∼0.1–1 kpc) region. In this case, any star-forming signature would be missed by spatially resolved image studies that always exclude the central region as a result of subtracting the diffracted nuclear light. The large extinction in the circumnuclear region can also hide star formation traced by extinction-sensitive probes (e.g., UV emission & [OII]λ3727 lines; Akiyama 2005; Ho 2005; Kim et al. 2006). Current examples of direct detections of intense circumnuclear starbursts in type-1 quasars are limited to a few nearby objects (Cresci et al. 2004). High-resolution molecular gas mapping has revealed a large gas concentration in the circumnuclear region for tens of quasars (Solomon & Vanden Bout 2005; Maiolino et al. 2007; Riechers et al. 2009; Walter et al. 2009). As the low-luminosity counterparts of quasars, nearby Seyfert galaxies frequently harbor circumnuclear starbursts (Heckman et al. 1997; Gu et al. 2001; González Delgado et al. 2001; Cid Fernandes et al. 2004; Davies et al. 2007; Riffel et al. 2009), although enhanced star formation also occurs in the spiral disks of Seyfert 2 galaxies (Maiolino et al. 1995). Quasars, with higher luminosity and thus larger mass inflow, probably harbor more intense circumnuclear starbursts. As shown in Figure 7(b), quasar hosts have on average LIRG-level SFRs. In normal local galaxies, such intense star formation is normally achieved only in the circumnuclear region (for a review, see Kennicutt 1998).

5.2.2. Comparisons with the Study of Stellar Populations

Studies of stellar populations through broadband SEDs and optical spectra have discovered intermediate-age stars or bluer colors in AGN hosts compared to their inactive galaxy counterparts at both low redshift (Ronnback et al. 1996; Brotherton et al. 1999; Kauffmann et al. 2003a; Jahnke & Wisotzki 2003; Jahnke et al. 2004; Canalizo et al. 2006; Vanden Berk et al. 2006; Jahnke et al. 2007; Schawinski et al. 2009) and high redshift (Ammons et al. 2009). In the following, we show that the spectral features employed by current studies of stellar populations are not sensitive to ongoing (<0.1 Gyr) starburst activity.

The continuum shape is useful to detect the presence of the young stellar population only if the spectrum extends shorter than 4000 Å or the broadband SED includes *U* band. At low redshift, it is difficult to achieve good coverage of the spectrum/SED at such short wavelengths. Thus our result of enhanced SFRs does not contradict studies based on the continuum shape at $\lambda > 4000$ Å that detect intermediate-age stellar populations (Ronnback et al. 1996; Jahnke & Wisotzki 2003; Jahnke et al. 2004; Schawinski et al. 2009; Ammons et al. 2009). On the other hand, at $\lambda < 4000$ Å the contrast between nuclear- and host-light in type-1 AGNs becomes much higher compared to the value at redder wavelengths. The subtraction of the nuclear light always introduces large errors on the resulting host brightness. Even in type-2 AGNs, the scattered nuclear UV light is sometimes important or even dominates (Zakamska et al. 2006). More importantly, obscuration can hide blue host-galaxy light if star formation occurs in the circumnuclear region as discussed above. Therefore, results based on spectra extending shorter than < 4000 Å may still underestimate significantly the level of ongoing star formation activity (Jahnke et al. 2007; Vanden Berk et al. 2006; Chen et al. 2009).

Kauffmann et al. (2003a) employed the 4000 Å break and Hδ absorption to study stellar populations and found intermediate-age stars in hosts with early-type morphologies. The 4000 Å break is caused by metal line absorptions. In hot stars with age < 0.1 Gyr (see Figure 2 of Kauffmann et al. 2003b), the 4000 Å break is small (<1.15) and insensitive to the stellar age. Moreover, the 4000 Å break is a luminosity-weighted mean-age indicator and thus does not have the temporal resolution to separate young stars from dominant old stars in a massive host galaxy. Hδ absorption arises in late-B to early-F stars and is thus only prominent 0.1–1 Gyr after star formation (Kauffmann et al. 2003b). Therefore, the two probes are not sensitive to ongoing star formation activity. In addition, stellar-age-dependent obscuration may also completely hide the effect of massive OB stars on these two features. In fact, such selective obscuration may be the reason for the presence of some LIRGs whose optical spectra show strong Hδ absorption but weak O[II] emission (Poggianti & Wu 2000). Studies based on the whole SDSS spectrum suffer from similar problems (Jahnke et al. 2007; Vanden Berk et al. 2006; Wild et al. 2007; Chen et al. 2009), as the continuum shape may be affected by extinction and nuclear light contamination while all the available stellar features (Balmer break, high-order Balmer absorption line, 4000 Å break and Ca II (H&K)) are not sensitive to the current star formation whose characteristic features (mainly nebular emission lines) are contaminated severely by the nuclear radiation in both type-1 and type-2 objects.

In summary, by integrating different studies, we now have a more complete census of the stellar population in type-1 quasar hosts, which appear to be massive galaxies presumably dominated by old stars, but that harbor a significant fraction (10%) of intermediate-age stellar populations, and are experiencing intense circumnuclear star formation.

5.3. Implications for the BH–Bulge Correlation

The direct measurements of SFRs in quasar hosts can provide new insights into the mechanism that shapes the $M_{\rm BH}$–σ relationship. Figure 7(c) shows the redshift evolution for the ratio of the SFR in quasar hosts to the black hole growth rate, obtained by dividing the integral SFIR LF by the integral BH growth rate function. The SFIR luminosity is converted to the SFR using the Rieke et al. (2009) relations as shown above.

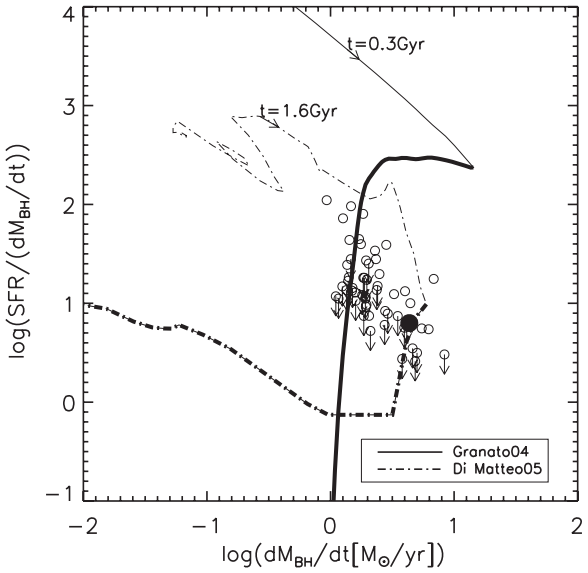

Figure 10. Ratio of the SFR and the BH accretion rate vs. the BH accretion rate. The open circles show the results for our $z \sim 1$ quasars and the filled circle is the mean value derived from the luminosity function. Curves show these two quantities along the merging process in two models, where the solid line is for the model in Granato et al. (2004) and the dot-dashed line is for the model in Di Matteo et al. (2005). The thick part of the curve indicates the stage after the peak BH accretion rate (presumably the type-1 quasar phase).

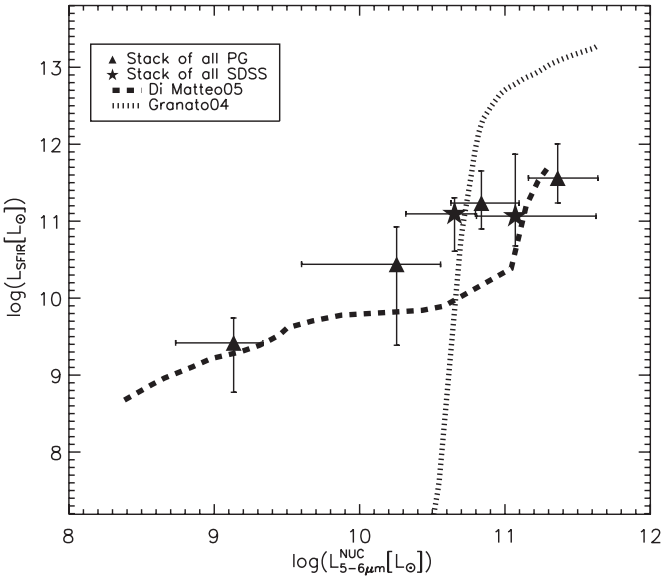

Figure 11. Correlation between the star-forming IR luminosity and the nuclear luminosity at 5–6 μm for the stacked spectra of all PG and SDSS quasars within certain 5–6 μm luminosity ranges as indicated by their error-bars on the X-axis. These are compared to the predictions of the model of Di Matteo et al. (2005) and that of Granato et al. (2004) shown as dashed and dotted lines, respectively.

The BH growth rate function is obtained from the quasar B-band LF using $L_{\rm bol} = \varepsilon/(1-\varepsilon)\dot{M}_{\rm BH}c^2 = c_B L_B$, where $L_{\rm bol}$ is the bolometric luminosity, ε is the mass to energy conversion efficiency, $\dot{M}_{\rm BH}$ is the BH growth rate and c_B is the bolometric correction for the B-band luminosity L_B. Figure 7(c) shows the result for $\varepsilon = 0.1$ and $c_B = 11.8$, where the quasar B-band LFs are given by Schmidt & Green (1983), and Richards et al. (2006). As shown in the figure, the SFR/$\dot{M}_{\rm BH}$ in quasar hosts is almost constant with redshift and has a value of $\sim$10, much lower than that expected from the $M_{\rm BH}$—σ relationship. This result rules out the simple model that the BH accretion and star formation evolve with a fixed ratio as given by the $M_{\rm BH}$—σ relation at any time for individual objects. This implies that $M_{\rm BH}/M_*$ for type-1 quasars deviates from that implied by the $M_{\rm BH}$–σ relation. The factor of deviation of $M_{\rm BH}/M_*$ can be given roughly as $(1+\Delta M_{\rm BH}/M_{\rm BH})$=exp$(\eta \frac{t_{\rm qso}}{4.4\times10^7{\rm yr}})$, where η is the fractional Eddington accretion rate $\eta = \dot{M}_{\rm acc}/\dot{M}^{\rm EDD}_{\rm acc}$ and $t_{\rm qso}$ is the duration of the type-1 quasar phase in years. For $\eta =$ (0.1–1) and $t_{\rm qso} = 10^8$ yr, the deviation is a factor of 1–10.

Numerical simulations have invoked galaxy mergers and quasar feedback to successfully explain the $M_{\rm BH}$–σ relationship (Granato et al. 2004; Di Matteo et al. 2005). Different models predict different time evolution of the SFR and BH accretion rate along the merging process. Our direct measurements of SFRs in type-1 quasars can provide constrains on these models. Our $z \sim 1$ quasars have a median BH mass of $10^{8.9\pm0.3}$ $M_\odot$ (Shen et al. 2008). In Figure 10, we compare our result to the model of Granato et al. (2004) for their most massive dark matter halo and the model of Di Matteo et al. (2005) for their most massive galaxy. For each model, the thicker part of the curve indicates the stage after the peak BH accretion rate, presumably the type-1 quasar phase. The open circles show the results for our $z \sim 1$ quasars and the filled circle is the mean value derived from the LF. As shown in Figure 10, individual quasars span a range of $\dot{M}_{\rm BH}$ and SFR/$\dot{M}_{\rm BH}$. For the model of Granato et al. (2004), the full range of the SFR/$\dot{M}_{\rm BH}$ resides within their type-1 quasar phase. However, the SFR in the model is more than an order of magnitude higher than our average value (the filled circle). Di Matteo et al. (2005) produced a model with the mean $\dot{M}_{\rm BH}$ and SFR/$\dot{M}_{\rm BH}$ comparable to our observed result. The much higher SFR in Granato et al. (2004) may be related to their high star formation efficiency which is determined by the free-fall or cooling time in their models, while in the Di Matteo et al. (2005) star formation occurs in a self-regulated mode.

In Figure 11, we further compare our $L_{\rm SFIR}$–$L^{\rm NUC}_{5-6\,\mu{\rm m}}$ relationship to predictions of these two models. As models only produce the average case, we here use the $L_{\rm SFIR}$–$L^{\rm NUC}_{5-6\,\mu{\rm m}}$ relation determined from the composite spectra of all PG and SDSS quasars within certain luminosity ranges. The SFRs of the two models are converted to the SFIR luminosity using the Rieke et al. (2009) relationship. The BH accretion rate is first converted to the bolometric luminosity by assuming $L_{\rm bol} = \varepsilon/(1-\varepsilon)\dot{M}_{\rm BH}c^2$ and $\varepsilon = 0.1$. The resulting bolometric luminosity is converted to $L^{\rm NUC}_{5-6\,\mu{\rm m}}$ based on the $L_{\rm bol}$–$L^{\rm NUC}_{5-6\,\mu{\rm m}}$ relationship of our SDSS sample whose bolometric luminosity is taken from Shen et al. (2008). Only the type-1 stage (i.e., after the peak BH accretion rate) of the two models is shown in Figure 11. The model of Di Matteo et al. (2005) is generally consistent with our observed relationship with a bit lower slope, while Granato et al. (2004) predict a much steeper slope. This implies that the quasar feedback may be overestimated significantly in Granato et al. (2004). The feedback energy in Di Matteo et al. (2005) is fixed to be 0.5% of the accreted rest mass energy while this fraction in Granato et al. (2004) is several times higher.

6. CONCLUSIONS

To constrain the cosmic evolution of star formation in quasar host galaxies, we present *Spitzer* IRS observations of a complete SDSS sample of 57 type-1 quasars at $z \sim 1$. The main conclusions are as follows.

1. About half of the sample has aromatic features detected at 6.2 and/or 7.7 μm. The composite profile of these two

features is similar to those of normal galaxies, ULIRGs and AGNs at both low and high redshift, implying star formation excitation of the aromatic features at $z \sim 1$.

2. Based on the aromatic-to-SFR ratio of star-forming galaxies at $z \sim 1$, we have constructed the SFIR LF of $z \sim 1$ type-1 quasars. Similar to low-redshift PG quasars, these $z \sim 1$ quasars show a flatter SFIR LF than $z \sim 1$ field galaxies, implying the quasar host galaxy population has on average higher SFRs. Based on the measured SFIR LF, individual quasar hosts are shown to be experiencing on average LIRG-level SFRs, which most likely occur in the circumnuclear region.
3. By comparing with similar measurements of low-redshift PG quasars, we found that the comoving SFIR energy density in type-1 quasar hosts shows much faster evolution than that in field galaxies, while the average SFR and the average SFR/$\dot{M}_{\rm acc}$ ratio are almost constant with redshift.
4. For individual objects, we have found a correlation between the aromatic-based SFR and the nuclear luminosity. By comparing this result to predictions of different models, we have found that the model in Granato et al. (2004) may overestimate the quasar feedback significantly while the model in Di Matteo et al. (2005) produces a roughly consistent result.
5. By combining different studies in the literature, we now have a more complete view of the stellar population in type-1 quasar hosts, which reside in massive galaxies with dominant old stars, harbor a significant fraction (∼10%) of intermediate-age stellar populations and are experiencing intense star formation.

We thank the anonymous referee for the detailed and constructive comments. We also thank Jane Rigby and Dean Hines for careful reading and comments. Support for this work was provided by NASA through contract 1255094 issued by JPL/California Institute of Technology.

REFERENCES

Akiyama, M. 2005, ApJ, 629, 72
Aller, M. C., & Richstone, D. 2002, AJ, 124, 3035
Alonso-Herrero, A., Pérez-González, P. G., Rieke, G. H., Alexander, D. M., Rigby, J. R., Papovich, C., Donley, J. L., & Rigopoulou, D. 2008, ApJ, 677, 127
Ammons, S. M., Melbourne, J., Max, C. E., Koo, D. C., & Rosario, D. J. V. 2009, AJ, 137, 470
Bahcall, J. N., Kirhakos, S., Saxe, D. H., & Schneider, D. P. 1997, ApJ, 479, 642
Bennert, N., Canalizo, G., Jungwiert, B., Stockton, A., Schweizer, F., Peng, C. Y., & Lacy, M. 2008, ApJ, 677, 846
Bertram, T., Eckart, A., Fischer, S., Zuther, J., Straubmeier, C., Wisotzki, L., & Krips, M. 2007, A&A, 470, 571
Brand, K., et al. 2008, ApJ, 673, 119
Brandl, B. R., et al. 2006, ApJ, 653, 1129
Brotherton, M. S., et al. 1999, ApJ, 520, L87
Canalizo, G., Bennert, N., Jungwiert, B., Stockton, A., Schweizer, F., Lacy, M., & Peng, C. 2007, ApJ, 669, 801
Canalizo, G., & Stockton, A. 2001, ApJ, 555, 719
Canalizo, G., Stockton, A., Brotherton, M. S., & Lacy, M. 2006, New Astron. Rev., 50, 650
Chen, Y.-M., Wang, J.-M., Yan, C.-S., Hu, C., & Zhang, S. 2009, ApJ, 695, L130
Cid Fernandes, R., Gu, Q., Melnick, J., Terlevich, E., Terlevich, R., Kunth, D., Rodrigues Lacerda, R., & Joguet, B. 2004, MNRAS, 355, 273
Cresci, G., Maiolino, R., Marconi, A., Mannucci, F., & Granato, G. L. 2004, A&A, 423, L13
Cutri, R. M., Nelson, B. O., Francis, P. J., & Smith, P. S. 2002, in IAU Colloq. 184, AGN Surveys, ed. R. F. Green, E. Ye. Khachikian, & D. B. Sanders (ASP Conf. Proc. 284; San Francisco, CA: ASP), 127
Dale, D. A., & Helou, G. 2002, ApJ, 576, 159
Davies, R. 2008, New Astron. Rev., 52, 307
Davies, R. I., Mueller Sánchez, F., Genzel, R., Tacconi, L. J., Hicks, E. K. S., Friedrich, S., & Sternberg, A. 2007, ApJ, 671, 1388
Di Matteo, T., Springel, V., & Hernquist, L. 2005, Nature, 433, 604
Dunlop, J. S., McLure, R. J., Kukula, M. J., Baum, S. A., O'Dea, C. P., & Hughes, D. H. 2003, MNRAS, 340, 1095
Engelbracht, C. W., Rieke, G. H., Gordon, K. D., Smith, J.-D. T., Werner, M. W., Moustakas, J., Willmer, C. N. A., & Vanzi, L. 2008, ApJ, 678, 804
Evans, A. S., Solomon, P. M., Tacconi, L. J., Vavilkin, T., & Downes, D. 2006, AJ, 132, 2398
Falomo, R., Kotilainen, J. K., Pagani, C., Scarpa, R., & Treves, A. 2004, ApJ, 604, 495
Falomo, R., Treves, A., Kotilainen, J. K., Scarpa, R., & Uslenghi, M. 2008, ApJ, 673, 694
Farrah, D., et al. 2008, ApJ, 677, 957
Ferrarese, L., & Merritt, D. 2000, ApJ, 539, L9
Floyd, D. J. E., Kukula, M. J., Dunlop, J. S., McLure, R. J., Miller, L., Percival, W. J., Baum, S. A., & O'Dea, C. P. 2004, MNRAS, 355, 196
Fu, H., & Stockton, A. 2009, ApJ, 696, 1693
Gebhardt, K., et al. 2000, ApJ, 539, L13
Genzel, R., et al. 1998, ApJ, 498, 579
Goldschmidt, P., Miller, L., La Franca, F., & Cristiani, S. 1992, MNRAS, 256, 65
González Delgado, R. M., Heckman, T., & Leitherer, C. 2001, ApJ, 546, 845
Granato, G. L., De Zotti, G., Silva, L., Bressan, A., & Danese, L. 2004, ApJ, 600, 580
Gu, Q. S., Huang, J. H., de Diego, J. A., Dultzin-Hacyan, D., Lei, S. J., & Benítez, E. 2001, A&A, 374, 932
Guyon, O., Sanders, D. B., & Stockton, A. 2006, ApJS, 166, 89
Hatziminaoglou, E., et al. 2008, MNRAS, 386, 1252
Heckman, T. M., Gonzalez-Delgado, R., Leitherer, C., Meurer, G. R., Krolik, J., Wilson, A. S., Koratkar, A., & Kinney, A. 1997, ApJ, 482, 114
Hernán-Caballero, A., et al. 2009, MNRAS, 395, 1695
Ho, L. C. 2005, ApJ, 629, 680
Houck, J. R., et al. 2005, ApJ, 622, L105
Hughes, D. H., Kukula, M. J., Dunlop, J. S., & Boroson, T. 2000, MNRAS, 316, 204
Hutchings, J. B., Crampton, D., & Campbell, B. 1984, ApJ, 280, 41
Hutchings, J. B., Maddox, N., Cutri, R. M., & Nelson, B. O. 2003, AJ, 126, 63
Hyvönen, T., Kotilainen, J. K., Örndahl, E., Falomo, R., & Uslenghi, M. 2007, A&A, 462, 525
Jahnke, K., Kuhlbrodt, B., & Wisotzki, L. 2004, MNRAS, 352, 399
Jahnke, K., & Wisotzki, L. 2003, MNRAS, 346, 304
Jahnke, K., Wisotzki, L., Courbin, F., & Letawe, G. 2007, MNRAS, 378, 23
Jester, S., et al. 2005, AJ, 130, 873
Kauffmann, G., et al. 2003a, MNRAS, 346, 1055
Kauffmann, G., et al. 2003b, MNRAS, 341, 33
Kelly, B. C. 2007, ApJ, 665, 1489
Kennicutt, R. C., Jr. 1998, ARA&A, 36, 189
Kim, M., Ho, L. C., & Im, M. 2006, ApJ, 642, 702
Kormendy, J., & Richstone, D. 1995, ARA&A, 33, 581
Kotilainen, J. K., Falomo, R., Labita, M., Treves, A., & Uslenghi, M. 2007, ApJ, 660, 1039
Kotilainen, J. K., & Ward, M. J. 1994, MNRAS, 266, 953
Kukula, M. J., Dunlop, J. S., McLure, R. J., Miller, L., Percival, W. J., Baum, S. A., & O'Dea, C. P. 2001, MNRAS, 326, 1533
Lacy, M., Sajina, A., Petric, A. O., Seymour, N., Canalizo, G., Ridgway, S. E., Armus, L., & Storrie-Lombardi, L. J. 2007, ApJ, 669, L61
Le Floc'h, E., et al. 2005, ApJ, 632, 169
Lutz, D., et al. 2008, ApJ, 684, 853
Magnelli, B., Elbaz, D., Chary, R. R., Dickinson, M., Le Borgne, D., Frayer, D. T., & Willmer, C. N. A. 2009, A&A, 496, 57
Magorrian, J., et al. 1998, AJ, 115, 2285
Maiolino, R., Ruiz, M., Rieke, G. H., & Keller, L. D. 1995, ApJ, 446, 561
Maiolino, R., et al. 2007, A&A, 472, L33
Marble, A. R., Hines, D. C., Schmidt, G. D., Smith, P. S., Surace, J. A., Armus, L., Cutri, R. M., & Nelson, B. O. 2003, ApJ, 590, 707
Marconi, A., Risaliti, G., Gilli, R., Hunt, L. K., Maiolino, R., & Salvati, M. 2004, MNRAS, 351, 169
McLeod, K. K., & Rieke, G. H. 1995, ApJ, 454, L77
Mickaelian, A. M., Gonçalves, A. C., Véron-Cetty, M. P., & Véron, P. 2001, Astrophys., 44, 14

Murphy, E. J., Chary, R.-R., Alexander, D. M., Dickinson, M., Magnelli, B., Morrison, G., Pope, A., & Teplitz, H. I. 2009, ApJ, 698, 1380
Netzer, H., et al. 2007, ApJ, 666, 806
Nolan, L. A., Dunlop, J. S., Kukula, M. J., Hughes, D. H., Boroson, T., & Jimenez, R. 2001, MNRAS, 323, 308
Ogle, P., Whysong, D., & Antonucci, R. 2006, ApJ, 647, 161
Page, M. J., & Carrera, F. J. 2000, MNRAS, 311, 433
Pérez-González, P. G., et al. 2005, ApJ, 630, 82
Poggianti, B. M., & Wu, H. 2000, ApJ, 529, 157
Richards, G. T., et al. 2001, AJ, 121, 2308
Richards, G. T., et al. 2006, AJ, 131, 2766
Riechers, D. A., Walter, F., Carilli, C. L., & Lewis, G. F. 2009, ApJ, 690, 463
Rieke, G. H., Alonso-Herrero, A., Weiner, B. J., Pérez-González, P. G., Blaylock, M., Donley, J. L., & Marcillac, D. 2009, ApJ, 692, 556
Riffel, R. A., Storchi-Bergmann, T., Dors, O. L., & Winge, C. 2009, MNRAS, 393, 783
Rigby, J. R., et al. 2008, ApJ, 675, 262
Ronnback, J., van Groningen, E., Wanders, I., & Öumlrndahl, E. 1996, MNRAS, 283, 282
Roussel, H., Sauvage, M., Vigroux, L., & Bosma, A. 2001, A&A, 372, 427
Sajina, A., Yan, L., Armus, L., Choi, P., Fadda, D., Helou, G., & Spoon, H. 2007, ApJ, 664, 713
Schawinski, K., Virani, S., Simmons, B., Urry, C. M., Treister, E., Kaviraj, S., & Kushkuley, B. 2009, ApJ, 692, L19
Schmidt, M., & Green, R. F. 1983, ApJ, 269, 352
Schweitzer, M., et al. 2006, ApJ, 649, 79
Scoville, N. Z., Frayer, D. T., Schinnerer, E., & Christopher, M. 2003, ApJ, 585, L105
Shankar, F., Salucci, P., Granato, G. L., De Zotti, G., & Danese, L. 2004, MNRAS, 354, 1020
Shen, Y., Greene, J. E., Strauss, M. A., Richards, G. T., & Schneider, D. P. 2008, ApJ, 680, 169
Shi, Y., Rieke, G., Lotz, J., & Perez-Gonzalez, P. G. 2009, ApJ, 697, 1764
Shi, Y., et al. 2006, ApJ, 653, 127
Shi, Y., et al. 2007, ApJ, 669, 841
Silverman, J. D., et al. 2009, ApJ, 696, 396
Smith, E. P., Heckman, T. M., Bothun, G. D., Romanishin, W., & Balick, B. 1986, ApJ, 306, 64
Smith, J. D. T., et al. 2007, ApJ, 656, 770
Sobral, D., et al. 2009, MNRAS, 398, 75
Solomon, P. M., & Vanden Bout, P. A. 2005, ARA&A, 43, 67
Soltan, A. 1982, MNRAS, 200, 115
Spoon, H. W. W., Marshall, J. A., Houck, J. R., Elitzur, M., Hao, L., Armus, L., Brandl, B. R., & Charmandaris, V. 2007, ApJ, 654, L49
Sturm, E., Hasinger, G., Lehmann, I., Mainieri, V., Genzel, R., Lehnert, M. D., Lutz, D., & Tacconi, L. J. 2006, ApJ, 642, 81
Teplitz, H. I., et al. 2007, ApJ, 659, 941
Urrutia, T., Lacy, M., & Becker, R. H. 2008, ApJ, 674, 80
Valiante, E., Lutz, D., Sturm, E., Genzel, R., Tacconi, L. J., Lehnert, M. D., & Baker, A. J. 2007, ApJ, 660, 1060
Vanden Berk, D. E., et al. 2001, AJ, 122, 549
Vanden Berk, D. E., et al. 2006, AJ, 131, 84
Walter, F., Riechers, D., Cox, P., Neri, R., Carilli, C., Bertoldi, F., Weiss, A., & Maiolino, R. 2009, Nature, 457, 699
Watabe, Y., Risaliti, G., Salvati, M., Nardini, E., Sani, E., & Marconi, A. 2009, MNRAS, 396, L1
Wang, R., et al. 2008, ApJ, 687, 848
Weedman, D. W., Le Floc'h, E., Higdon, S. J. U., Higdon, J. L., & Houck, J. R. 2006, ApJ, 638, 613
Wild, V., Kauffmann, G., Heckman, T., Charlot, S., Lemson, G., Brinchmann, J., Reichard, T., & Pasquali, A. 2007, MNRAS, 381, 543
Wisotzki, L., Christlieb, N., Bade, N., Beckmann, V., Köhler, T., Vanelle, C., & Reimers, D. 2000, A&A, 358, 77
Wu, H., Cao, C., Hao, C.-N., Liu, F.-S., Wang, J.-L., Xia, X.-Y., Deng, Z.-G., & Young, C. K.-S. 2005, ApJ, 632, L79
Yan, L., et al. 2007, ApJ, 658, 778
Yu, Q., & Tremaine, S. 2002, MNRAS, 335, 965
Zakamska, N. L., Gómez, L., Strauss, M. A., & Krolik, J. H. 2008, AJ, 136, 1607
Zakamska, N. L., et al. 2006, AJ, 132, 1496